# IZMIR KATIP CELEBI UNIVERSITY

# GRADUATE SCHOOL OF NATURAL AND APPLIED SCIENCES

# AERODYNAMIC DESIGN OF A NOVEL LOW PRESSURE COMPRESSION SYSTEM FOR VARIABLE-SPEED MICRO TURBOFAN

**M.Sc. THESIS**

**Menal İLHAN**

**Department of Mechanical Engineering**

**Thesis Advisor: Asst. Prof. Dr. Sercan ACARER**

**DECEMBER 2019**

# IZMIR KATIP CELEBI UNIVERSITY
# GRADUATE SCHOOL OF NATURAL AND APPLIED SCIENCES

## AERODYNAMIC DESIGN OF A NOVEL LOW PRESSURE COMPRESSION SYSTEM FOR VARIABLE-SPEED MICRO TURBOFAN

**M.Sc. THESIS**

**Menal İLHAN**

**(Y160217002)**

**Department of Mechanical Engineering**

**Thesis Advisor: Asst. Prof. Dr. Sercan ACARER**

**DECEMBER 2019**

# İZMİR KATİP CELEBİ ÜNİVERSİTESİ
# FEN BİLİMLERİ ENSTİTÜSÜ

## DEĞİŞKEN HIZLI MİCRO TURBOFAN İÇİN YENİLİKÇİ DÜŞÜK BASINÇLI KOMPRESÖR SİSTEMİNİN AERODİNAMİK TASARIMI

### YÜKSEK LİSANS TEZİ

**Menal İLHAN**

**(Y160217002)**

**Makine Mühendisliği Ana Bilim Dalı**

**Tez Danışmanı: Dr. Öğr. Üyesi Sercan ACARER**

**ARALIK 2019**

**Menal İLHAN**, a **M.Sc.** student of **IKCU Graduate School Of Natural And Applied Sciences**, successfully defended the thesis entitled "**Aerodynamic Design Of A Novel Low Pressure Compression System For Variable-Speed Micro Turbofan**", which she prepared after fulfilling the requirements specified in the associated legislations, before the jury whose signatures are below.

**Thesis Advisor :**

        **Asst. Prof. Dr. Sercan ACARER** .........................
        İzmir Kâtip Çelebi University

**Jury Members :**

        **Asst. Prof. Dr. Z. Haktan KARADENİZ** .........................
        İzmir Kâtip Çelebi University

        **Assoc. Prof. Dr. Ünver ÖZKOL** .........................
        İzmir Institute of Technology

**Date of Defense : 02.12.2019**

*To my family*

# FOREWORD

First and foremost, I would like to thank my advisor, Asst. Prof. Dr. Sercan ACARER for his advises, guidance, support, encouragement, and inspiration through the thesis. I would like to thank my family who have supported and encouraged me during my graduate studies.

December 2019

Menal İLHAN

# TABLE OF CONTENTS

# LIST OF TABLES

# LIST OF FIGURES

# ABBREVIATIONS

**UAV**          : Unmanned Aerial Vehicle

**CVT**          : Continuously Variable Transmission

**LPC**          : Low Pressure Compressor

**SFC**          : Specific Fuel Consumption

**GTF**          : Geared Turbofan Engines

**OPR**          : Overall Pressure Ratio

**IGV**          : Inlet Guide Vane

**TET**          : Turbine Entry Temperature

**CFD**          : Computational Fluid Dynamics

**RANS**         : Reynolds Average Navier-Stokes

**LPT**          : Low Pressure Turbine

**HPT**          : High Pressure Turbine

**SST**          : Shear Stress Transport

**RSM**          : Reynolds Stress Model

**LE**           : Leading Edge

**TE**           : Trailing Edge

**DCA**          : Double Circular Arc

**SS**           : Suction Side

**PS**           : Pressure Side

**BPR**          : Bypass ratio

# AERODYNAMIC DESIGN OF A NOVEL LOW PRESSURE COMPRESSION SYSTEM FOR VARIABLE-SPEED MICRO TURBOFAN

## ABSTRACT

Unmanned Aerial Vehicles (UAVs) are commonly propeller-driven and intended towards low-speed applications. Micro turbojet engines, on the other hand, has shorter ranges due to much higher rates of fuel consumption. The use of turbofans instead of turbojets are restricted due to price and complexity issues. To cope with this, a basic micro turbojet may be converted into a single spool turbofan without additional components of a booster and low pressure turbine. This is normally cause matching problems since two spools are required to adjust fan speed independently. A simpler solution may be to use a continuously variable transmission (CVT) gearbox that may be used to adjust optimal speed for the fan. Moreover, the positive functionality of the missing booster may be lumped into the fan root to form a unified low pressure compression system (unified-LPC), to the author's best knowledge, for the first time in the open literature.

Such unified-LPC has unique characteristics of having extreme twist, much higher pressure ratio and mass flux at the core than at the tip albeit lower root rotational speed. Correspondingly, many aerodynamic and structural problems arise. The former one includes the difficulty to design a unified fan and booster rotor within a single stage compressor. Moreover, this causes the necessity of a transonic and highly loaded stator design due to excessive root mass flux, which yields to high mixing losses downstream of the stator. This, combined with the high-area-ratio diffuser-shaped duct to connect the fan with the engine compressor, causes notable disability for the unified-LPC to pass the required pressurized air. The latter one includes the vibrational response of an excessively-twisted rotor. Most notably, a systematic existence of negative aerodynamic damping (flutter) may render the concept infeasible.

In light of these challenges, this thesis aims to investigate aerodynamic design options of such a unified-LPC. Initially, a detailed demonstration of the concept on a representative micro jet thermodynamic cycle is presented by meridional modeling. During this stage, key comparisons between two alternative configurations, the cases with and without inlet guide vanes (IGV), revealed the effect of major design choices on the performance. The more promising configuration is further investigated by experimentally validated CFD simulations to assess the actual potential of the concept. The next step focuses on the stator, which creates a serious performance

bottleneck due to the aforementioned downstream mixing losses. In order to address this, the performance of alternative stator concepts featuring excessively high hub solidity and three-dimensional aerodynamics (bow lean and sweep) are investigated. Detailed flow field results of the four stator cases reveal loss mechanisms.

# DEĞİŞKEN HIZLI MİCRO TURBOFAN İÇİN YENİLİKÇİ DÜŞÜK BASINÇLI KOMPRESÖR SİSTEMİNİN AERODİNAMİK TASARIMI

## ÖZET

İnsansız Hava Araçları (İHA) genellikle pervane tahrikli ve düşük hızlı uygulamalara yöneliktir. Mikro turbojet motorları ise çok daha yüksek yakıt tüketimine bağlı olarak daha kısa menzillere sahiptir. Fiyat ve karmaşıklık sorunları nedeniyle, turbofanlar yerine turbojetlerin kullanımı kısıtlanmaktadır. Bununla başa çıkabilmek için, temel bir mikro turbojet, ek (booster) kompresörü ve düşük basınçlı türbin bileşenleri olmadan tek milli turbofana dönüştürülebilir. Bu normalde eşleştirme sorunlarına neden olur çünkü fan hızını bağımsız olarak ayarlamak için iki mil gerekir. Daha basit bir çözüm olarak, fanın optimum hızını ayarlamak için sürekli değişken bir aktarma sistemi kullanılmaktadır. Takviye kompresörünün sağladığı olumlu işlevinin eksikliği fan kökünde toplanmış bir birleşik Düşük Basınç Kompresörü sistemi tasarımı ile giderilir. Bu konsept yazarların bilgisi dahilinde açık literatürde ilk kez uygulanmaktadır.

Bu birleşik düşük basınç kompresörü maximum itki ve verim elde edilecek şekilde tasarlanmalıdır. Bu sebeple core kısmındaki kanat yapısı bypass kısmındaki kanat yapısına göre aşırı büküme, çok yüksek basınç oranı ve kütle akışına sahip olması gereklidir. Buna bağlı olarak, birçok aerodinamik ve yapısal problem ortaya çıkmaktadır. Birincisi, tek kademeli bir kompresör içinde birleşik bir fan ve takviye kompresör konsepti tasarlama zorluğudur. Ayrıca, bu, statorun aşağısı akışında yüksek karışım kayıplarına neden olan aşırı kök kütlesel akışı nedeniyle bir transonik ve çok yüklü stator tasarımının gerekliliğine neden olmaktadır. Bu, fanı motor kompresörüne bağlamak için yüksek alan oranlı difüzör şeklindeki kanalla birleştiğinde, birleşik LPC'nin gereken basınçlı havayı geçmesi için önemli ölçüde engel oluşturur. Sonuncusu, aşırı bükülmüş bir rotorun titreşimsel tepkisini içerir. En önemlisi, negatif aerodinamik sönümlemenin (fluttern) sistematik varlığı uygulanabilir olmadığını gösterebilir.

Bu zorlukların ışığında, bu tez böyle bir birleşik LPC'nin aerodinamik tasarım seçeneklerini incelemeyi amaçlamaktadır. İlk olarak, temsili bir mikro jet termodinamik çevrimi üzerine konseptin ayrıntılı bir gösterimi meridional modelleme ile sunulmaktadır. Bu aşamada, iki alternatif konfigürasyon arasındaki anahtar karşılaştırmalar, giriş kılavuz kanatçığı olan ve olmayan (IGV) durumlar, büyük tasarım seçeneklerinin performans üzerindeki etkisini ortaya çıkardı. Daha umut vaat eden konfigürasyon, konseptin gerçek potansiyelini değerlendirmek için

deneysel olarak onaylanmış CFD simülasyonları ile daha fazla araştırılmaktadır. Bir sonraki adım, yukarıda bahsedilen akış aşağı karıştırma kayıplarından dolayı ciddi bir performans darboğazı yaratan statora odaklanmaktadır. Bunu ele almak için, aşırı yüksek göbek katılığı ve üç boyutlu aerodinamik (bow lean and sweep) içeren alternatif stator konseptlerinin performansı incelenmiştir. Dört stator durumu için ayrıntılı akış alanı sonuçları, kayıp mekanizmalarını ortaya koymaktadır.

# 1. INTRODUCTION

Unmanned aerial vehicles (UAV) have been widely used in recent years. These commonly used UAVs are generally intended for low speed applications. The propulsion is produced by an internal combustion engine that drives a propeller and is not suitable for high-speed flights due to this drive scheme using a reciprocating engine. Innovative engine solutions are required for the development of low-cost and high-speed UAVs for long-range flights in remote and difficult-to-access areas. Furthermore, thanks to these innovative engine solutions, it can make significant contributions in disaster situations, search and rescue operations, and in situations such as fire fighting.

Micro-turbojets can provide high thrust levels, but the range is limited due to low propulsive efficiency, ie high fuel consumption. For this reason, turbofan engines with higher propulsion efficiency are used on larger platforms. In recent years, studies in aero-motor efficiency have been carried out. The design and aerodynamic matching of the individual components in these studies are factors that make it difficult to design such complex systems. Engine-specific fuel consumption (SFC) is particularly adversely affected by the occurrence of uncontrolled tip leakages. To examine this, Toal et al. [1], demonstrated the feasibility of combining thermomechanical simulations with global optimization methods to minimize tip leakage of a turbofan high-pressure compressor. This study was made possible in terms of calculation by using a multi-fidelity simulation approach and meta-modeling methods. For the same realistic constraints and weights, an improvement of 3.44% was observed in SFC. In this study, the effect of tip leakages was seen on engine-specific fuel consumption.

Recuperation and inter cooling is another area of improvement. This is not a common option due to fuel prices, complexity, and high pressure losses so far. Goulas et al. [2] studied the feasibility of recuperation of a turbofan. In this study, experimental data, computational fluid dynamics (CFD) and cycle calculations are

used. A significant increase in SFC was observed when pressure losses were maintained at manageable levels in recuperation and coped with weight problems.

Xu et al. [4] studied the combined effects of recuperation and internal cooling in a turbofan, engine mechanical design, component maps, recuperator and intercooler losses, maximum external average temperature in high pressure turbine (HPT) blades, travel altitude, maximum low pressure turbine (LPT). They investigated the results of the study by a global optimizer combined with a conceptual design tool that takes into account the exit temperature, take-up distance constraints, and the time it takes to climb to low-pressure turbine field variability. The optimization for minimum SFC resulted in 5.56% healing for the recuperated and inter-cooled engine over the latest technology engine mainly by changing compressor and fan pressure ratios and varying stators in LPT.

Within a similar framework, Kyprianidis et al. [5-6] extended these studies to contemplate geared turbofan architecture (GTF) and emission aspects. As a result of these studies, it was observed that SFC decreased. The use of reverse-rotating turbomachinery components can improve SFC. Because of these aerodynamically and mechanical complexities, it has not been widely used so far.

New models have been developed by Alexiou et al. [7] to investigate the off-design features of a GTF with a counter-rotating core compressor and turbine, without

stators. SFC improvement is 0.59%. Although this improvement was marginal, the total SFC improvement was 3.2% due to a 10% weight reduction.

It has been suggested that the booster be driven by both HPT and LPT by a suitable gearbox, called "Dual Drive Enhancer" so that it will have a higher degree of freedom [8]. This study shows that the dual drive booster is a suitable concept. Also, the advantages and disadvantages were discussed. Kaiser et al. [9] introduced an engine concept to achieve radical improvements in engine efficiency. They tried to increase the total engine pressure ratio by more than 100 (high pressure ratio). An engine concept was selected based on the simplified parametric studies of the cycle, besides qualitative measures covering size, efficiency, weight, emissions, the life cycle and operational behavior. The engine reaches over 300 peak pressure rates at

maximum climbing conditions. Although there was a 31% increase in weight, there was a 15% improvement in SFC.

As can be seen from the studies examined above, most gas turbines have made great progress in recent years. However, there has not been enough progress in micro gas turbines. The selection of engines used in UAVs generally consists of turbojets rather than advanced turbofans. Simplicity and cost are the main concerns for these small engines where high performance requirements are required. Kadosh and Beni [10] examined the applicability, properties and performance of turbojet turbofan conversion. In this study, a continuously variable transmission (CVT) was used. A reduction in fuel consumption was observed.

Jeschke and Penkner [11] studied a gas generator approach to assist those in designing small jet engines that require high power density, as in UAVs. In this study, tip leakages and vanes are eliminated. This greatly increases thrust for a given weight. But this concept led to low efficiency.

## 1.1 Turbofan

In turbofan engine, thrust is obtained by by-passed air accelerated by a ducted fan driven by jet core and jet core stream. It is also called a by-pass engine or fanjet. The large fan in the front of the turbofan engine sucks the air inside and a large portion of the air is bypassed. While some of the air intakes are used to drive the jet engine in the core, the other large part of the air directed separately from a series of compressors and conducted through the nozzle without entering the combustion chamber. Therefore, the by-pass air provides more thrust at low speeds and makes the engine quieter. In these engines, most of the airflows from the outside of the core engine and is bypassed because the by-pass system increases the thrust of the engine without increasing the fuel consumption. This is attained by increasing the total mass flow, on the contrary, decreasing the velocity at the same total energy supply. This engine is commonly used in commercial aviation jets and civil aircraft. The schematic representation is shown in Figure 1.1.
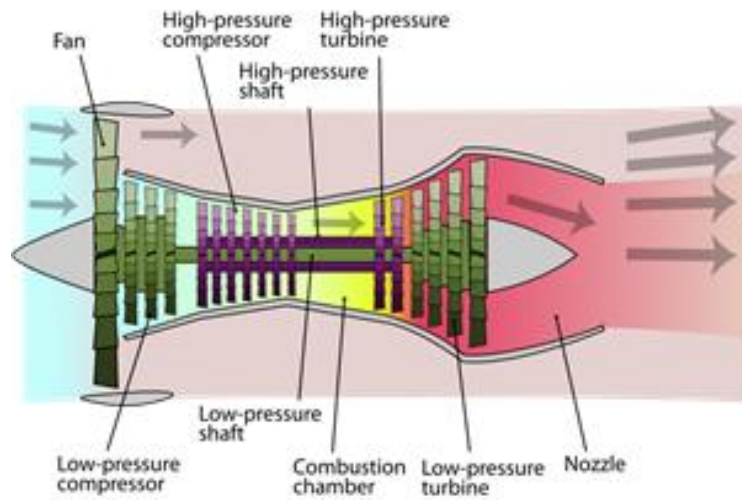
**Figure 1.1.** Turbofan engine

## 1.2 Turbojet

In turbojets, all of its thrust is produced by high energy gas flow from the exhaust nozzle. It is named as a core engine (gas generator) with a propelling nozzle. The operating principle of the turbojet engine is to achieve high thrust by increasing relatively less air mass to higher speeds. In such engines, when the air velocity approaches the aircraft speed (when the Mach number is approximately 2), it achieves the most efficient operating level. The turbojet engine is used in missiles and high speed military aircraft. The schematic representation is shown in Figure 1.2.
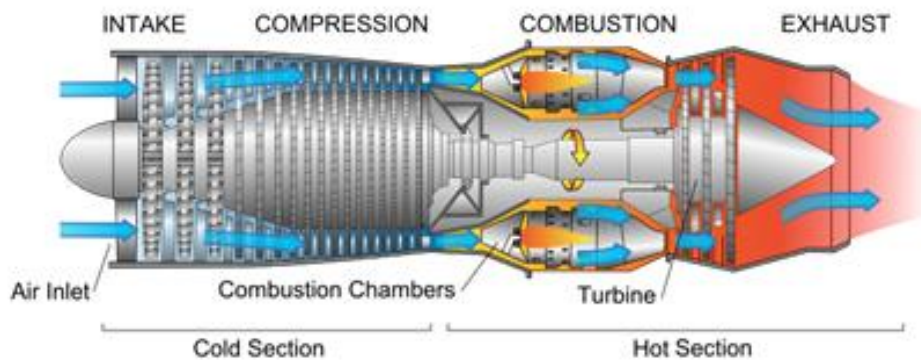


**Figure 1.2.** Turbojet engine

4

## 1.3 Thermodynamics of Gas Turbine Engine

Gas turbine engines are often used to generate power for a power plant or an aircraft or to produce the propulsion required for aircraft movement. They have four kinds of gas turbines engine including turbojet, turbofan, turboprop, and turboshaft. The common point of these gas turbine engines is the similarity in the thermodynamic cycle. A compressor is required for compression, a combustion chamber for combustion, and a turbine for generating power. The thermodynamic process needs to be known to understand what thrust or generate power is.

Brayton cycle is the thermodynamic cycle use in gas turbine engines. The Brayton cycle was originally developed for used in piston engines and is currently used mainly in gas turbine engines where compression and expansion processes take place.

Gas turbine engines generally work in an open cycle. Gas turbine engine cycle is given in Figure 1.3. For increase, the engine pressure fresh air is sucked by the compressor. This high pressure air is then burned at a constant pressure in the combustion chamber and its temperature increases. It then enters the turbine to obtain power from the energy of the gas having high temperature and pressure. The expanded gas exiting the turbine is delivered to the atmosphere through the nozzle. There is no circulation, and so the cycle is called open cycle.
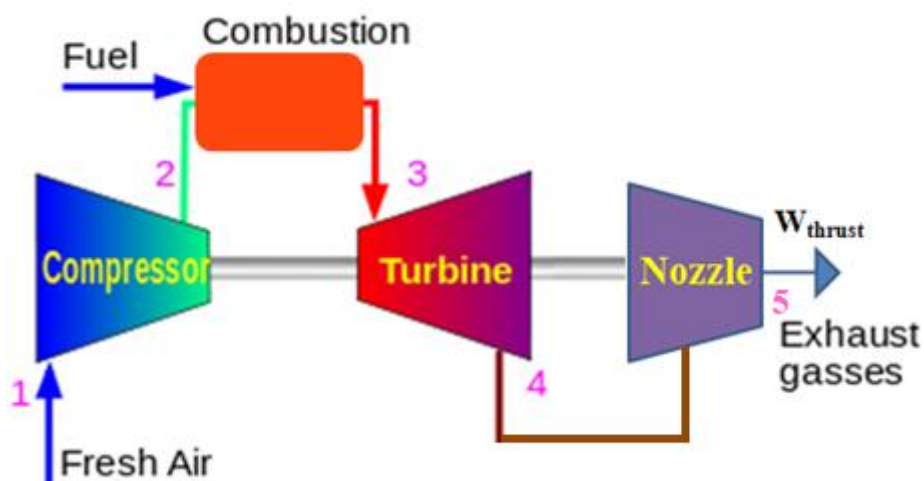


**Figure 1.3.** Gas turbine engine cycle

In this cycle;

1-2  : Compression Process

2-3  : Combustion Process

3-4  : Expansion Process

4-5  : Exhaust Process

## 1.4 Goal and Scope Definition

## 1.4.1 Motivation

In recent years, there has been no major progress in terms of performance and efficiency of micro-scale gas turbines. There is a lack of advanced micro-turbofan for UAVs. However, in recent studies, they have designed innovative, advanced and simple turbofan architecture suitable for small scale engines. This architecture is the conversion of an existing single shaft micro jet engine to a micro turbofan using a continuously variable transmission (CVT) due to limited design costs. This architecture was studied thermodynamically. In the preliminary studies, CVT was used for the connection of the low pressure compressor (LPC) which is the subject of this thesis and the core shaft. Also, versatility and maximum efficiency have been achieved by using a by-pass nozzle. The low pressure turbine (LPT) and booster found in typical larger turbofans were not used in this architecture. The HPT stage runs together with LPC and the core compressor. The basic representation of this architecture is as in Figure 1.4.
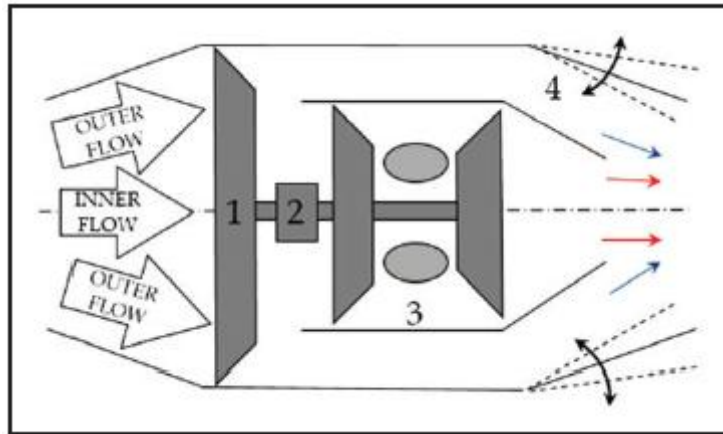
**Figure 1.4.** Schematic representation of the concept: (1) LPC (fan), (2) CVT, (3) gas generator without additional turbine, and (4) variable bypass nozzle

## 1.4.2 Scope of the current thesis

As already mentioned, the LPC system will be combined as a single stage axial compressor. This concept is an innovative design for the first time in the literature. It is expected to be a guide to micro turbofan concepts for future UAV engines. A comparison of this combined concept with a typical LPC system is given in Figure 1.5.
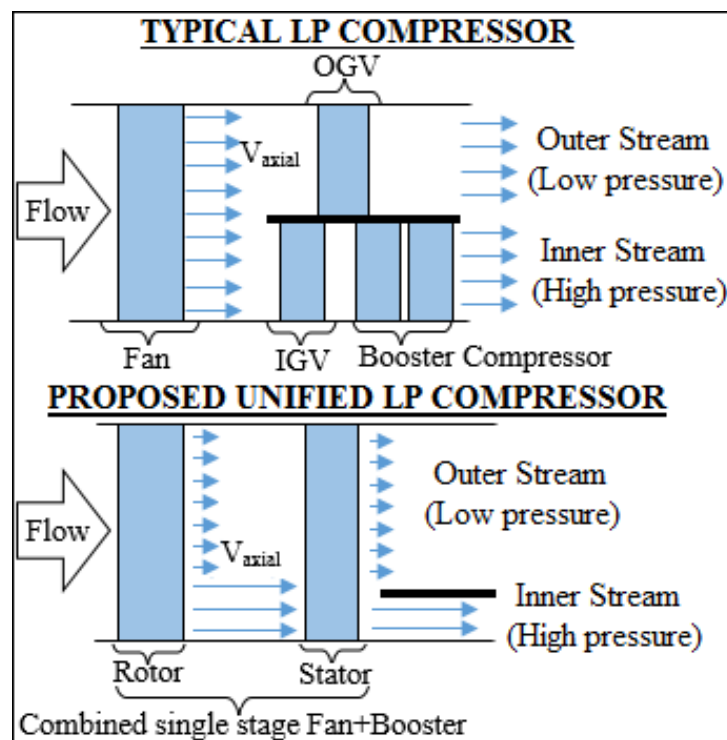


**Figure 1.5.** Comparison of conventional and recommended low pressure compressors for a similar bypass rate

Assuming that the performance maps down-scaled from existing large scale turbomachines, in this study, the applicability of the LPC system has been investigated by giving importance to the production and structure integrity of said micro-turbofan. In the preliminary thermodynamic cycle study for micro-turbofan in this study, it was seen that the thrusting process improved by more than 100%. There was also a significant improvement in SFC.

In the joint study by Palman et al. [12], the thermodynamic analysis made with the new system is discussed and the results of this study are given at the end of the study. Due to cost and efficiency limitations, the LPC features designed in this study are very different from the conventional booster and large-scale fan designs. In this concept, in order to contribute to the missing booster in the hub region, the new system must have a higher pressure ratio and mass flux/axial Mach in the hub of the fan compared to the tip region. Due to this difference in design, previously extrapolated performance maps can be misleading. Therefore, this study is expected to be a unique guide for future UAV engines.

In order to ensure repeatability in the new concept, no special design research or optimization studies are performed. Conventional hierarchical design methodology and some acknowledged rules, such as the employ of double circular arc (DCA) blading, feasible solidity values (lower than 3 at the hub and equivalent to relative Mach at the tip), relative thickness values (maximal 4% at the tip), and avoiding maximum diffusion limits (De-Haller bigger than 0.72 and equivalent diffusion factor lower than 2) are applied.

The new architecture with LPC will demand more work from the identical core turbine. When the inlet pressure to the core compressor is increased, both higher thermodynamic cycle efficiency and additional power from the turbine will be obtained. The fan root must be loaded additionally to compensate for the lack of booster, and the fan center and tip pressure ratio should be designed to minimize the lack of special shaft power and lack of booster compressor. Due to the need for increased work potential, a non-traditional design emerges. This design results in a highly twisted design with hub-loaded and tip-relaxed. This twist may be such that the rotor camber at the tip is substantially reduced, and even reversed. This results in

a significant increase in the axial velocity in the fan hub, and the opposite comes out at the fan mid and tip. This design differs from the typical loaded fan concept with much smoother pressure ratios and axial speeds [13]. For increase, the benefit to the thermodynamic cycle, the practical limits of the maximum difference between the bypass (outer) and core (inner) pressure ratios are examined. As a result of this rotor design, the downstream stator hub is highly loaded and becomes transonic. Furthermore, the core duct inlet area is greatly reduced as the hub axial speed increases. Normally the core duct inlet area requires an aggressive diffuser. Due to this reduction in the core duct inlet area and the strong stator downstream, the performance of the concept is greatly limited. These difficulties and considerations are shown in Figure 1.6.
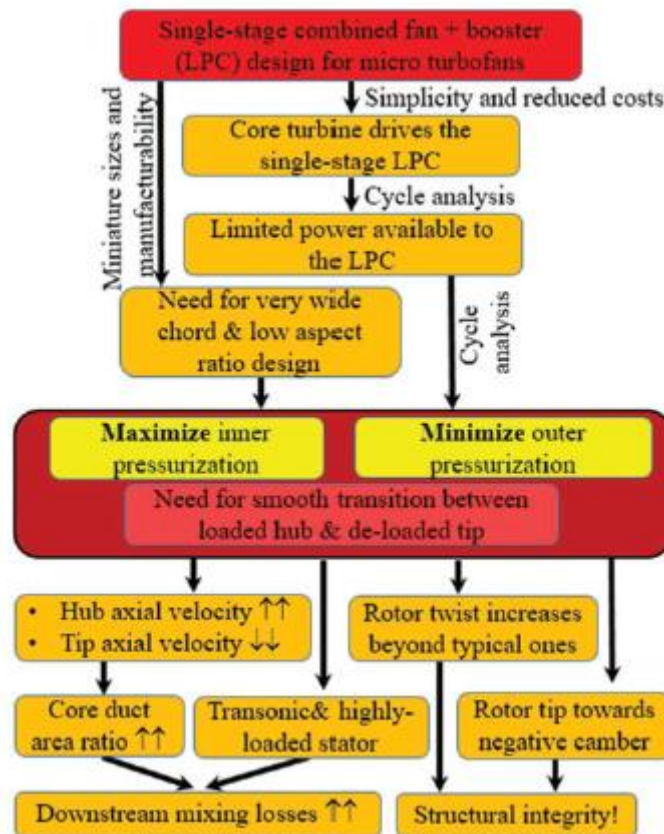


**Figure 1.6.** Considerations for the combined single-stage low pressure compression system

# 2. DESIGN OF THE FAN

## 2.1 Throughflow

For the aerodynamic design of the low pressure compressor system, an axisymmetric through-flow design code is used. Through-flow code is used for pre-design of fan stage, splitter, bypass and core ducts. The preliminary fan design is performed after many iterations with the high-fidelity flow.

Axial rotor and stator chords are critical points for the production of micro turbomachinery. Therefore, the first dimensions to be determined are the rotor and stator chords. Large chord lengths are important in ensuring proper blade thicknesses and reducing distorting viscous effects due to the increased Reynolds number. The relative thickness of the Titanium Alloy (Ti6Al4V ELI) with a yield stress of 930 MPa at max speed 35k rpm at the hub must be at least 16% for such highly-twisted fan. It has been found that in the preliminary flow simulations applicable to aerodynamic performance are achieved at these thickness levels.

The pressure ratio at the hub of the designed fan is higher than the mid/tip pressure ratio. Therefore, to maximize the pressure ratio at the hub, highly twisted and hub-loaded wide-chord / low-aspect-ratio rotor and a highly loaded wide-chorded transonic stator should be designed.

The fan must be designed according to the most critical operating condition. For this reason, the fan is designed according to the Take-Off condition where the rotation speed is highest. The following objectives have been determined in the take-off conditions for the fan system (Table 2.1).

**Table 2.1.** Preliminary design cycle requirements

|  | $\dot{m}$ [kg/s] | $\dot{m}_{outer}/\dot{m}_{inner}$ | $\Pi$ | $\eta_{isentropic}$ |
|---|---|---|---|---|
| Inner Stream | 1.25 | - | 1.6 | 0.80 |
| Outer Stream | 5.48 | - | 1.4 | 0.82 |
| Total | 6.73 | 4.38 | - | - |

The preliminary design code takes into account each blade section's chordwise loading location in embedded correlations through the parabolic camberline assumption. According to these embedded correlations, the camberline is the mid-loaded double circular arc (DCA) at the subsonic and transonic Mach numbers and aft-loaded multiple circular arcs at the supersonic Mach numbers. This through-flow code provides coupled modelling of bypass and core ducts separated by an aerodynamically shaped flow-splitter as well as the compression stage. Through-Flow model for the latest design is given in Figure 2.1. Total pressure ratio distribution for only rotor and stage are given in Figure 2.2.
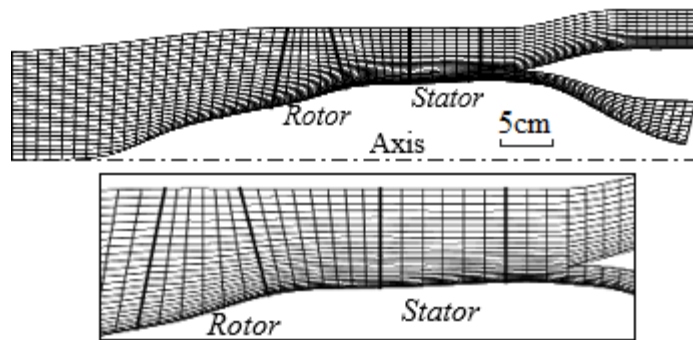
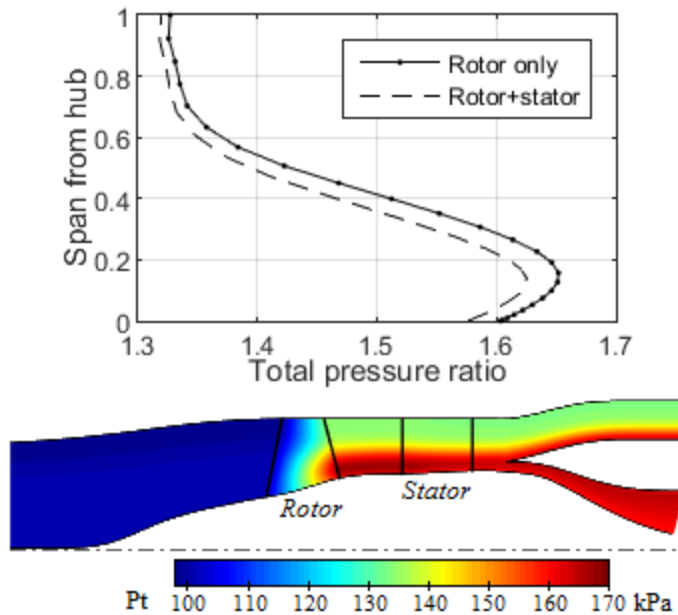**Figure 2.1.** Through-Flow Model for the Latest Design

**Figure 2.2.** Total Pressure Ratio Distribution

The small dimensions enforce the blade chords to be wide for feasible sufficiently large blade thicknesses. The resulting wide-chord design had an aspect (height/chord) ratio of unity as presented in the through-flow model (Figure 2.3).
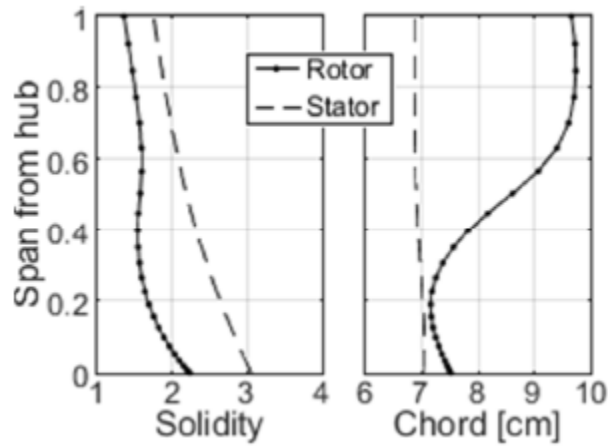
**Figure 2.3.** Solidity and chord distributions

After axial chords have been determined in accordance with the manufacture, the main diameters for the flow path are designed with the through-flow code. The cycle analysis using the minimized generic fan performance map used provides a take-off fan rotation speed of 29000 rpm. The actual design of this first take-off fan rotation speed estimation was calculated by taking into account the design of the bypass duct for a typical 20 cm diameter micro turbojet engine, and the desired diameter of 25 cm fan shroud. Therefore, this rotational speed value is kept unchanged. If this is at a higher shroud radius at the rotational speed, a tip Mach number would be bigger than 1.2 and would result in a reversed camber. This is not preferred for structural integrity and efficiency for the rotor having a low tip pressure ratio ($\prod_{total} = 1.4$) and a low tip working coefficient ($\psi_{tip}=\Delta H/(\omega r)^2 < 0.2$). Conversely, if there is a lower shroud radius, the inlet axial Mach number increases beyond 0.55-0.6 and also damages the bypass channel design.

The diameter of the fan inlet hub is determined to be 10 cm to maintain sufficient pitch distance between the two blades at a radius as small as possible and to ensure that the inlet axial Mach number is around 0.5. In cases where there is a high increase in hub diameter, the rotor aspect ratio decreases below unity. This results in stronger secondary flows and increases axial Mach number, which may create the blockage at the rotor hub. Because the rotor hub is the most loaded section, the diameter is increased from 10cm at the leading edge to 13.6cm at the trailing edge($\psi_{hub} = \Delta H/(\omega r)^2 \sim 1.34$, Figure 2.4). In this case, the stator hub turning is reduced. The diameter increase from the leading edge to the trailing edge was not be

linearized. End-Wall Contouring (EWC) is applied to improve aerodynamic performance. In order to minimize Mach number and to increase the choke limit, the hub endwall near the leading edge is designed as a concave shape. Near the trailing edge, it was designed as a convex shape to induced acceleration and reduced loading. Work coefficient distribution indicates a highly loaded compressor at the hub.
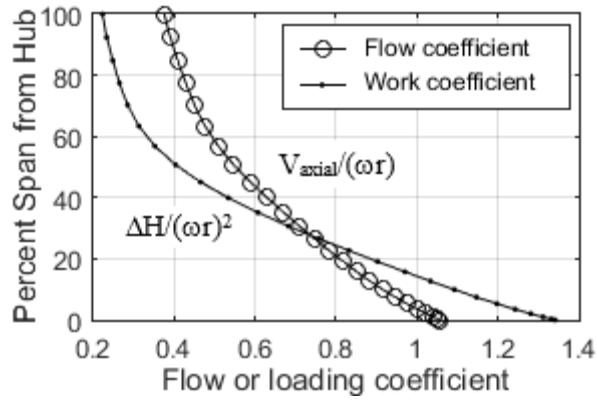


**Figure 2.4.** Flow and work coefficients for the fan rotor

Flow and work coefficients for the fan rotor are given in Figure 2.4.

The flow coefficient is as can be seen in Equation 2.1.

$$\Phi = \frac{V_{axial}}{\omega r} \tag{2.1}$$

and the work coefficient is can be seen in Equation 2.2.

$$\psi = \frac{\Delta H}{(\omega r)^2} \tag{2.2}$$
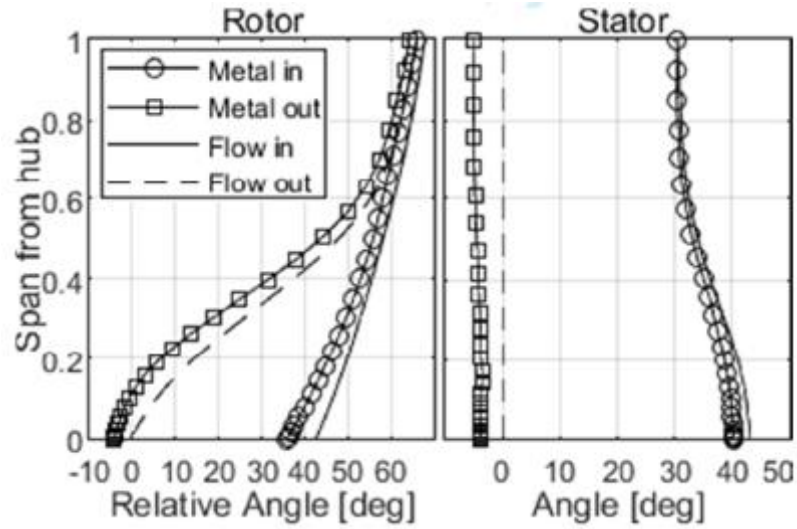
**Figure 2.5.** Flow and metal angles

The number of the rotor (11 blades) and stator (20 blades) blades were determined by deviation values (metal exit angle). Flow and metal angles from hub to tip are shown in Figure 2.5.

Resulting Equivalent Diffusion Factor and De-Haller from hub to tip are shown in Figure 2.6.
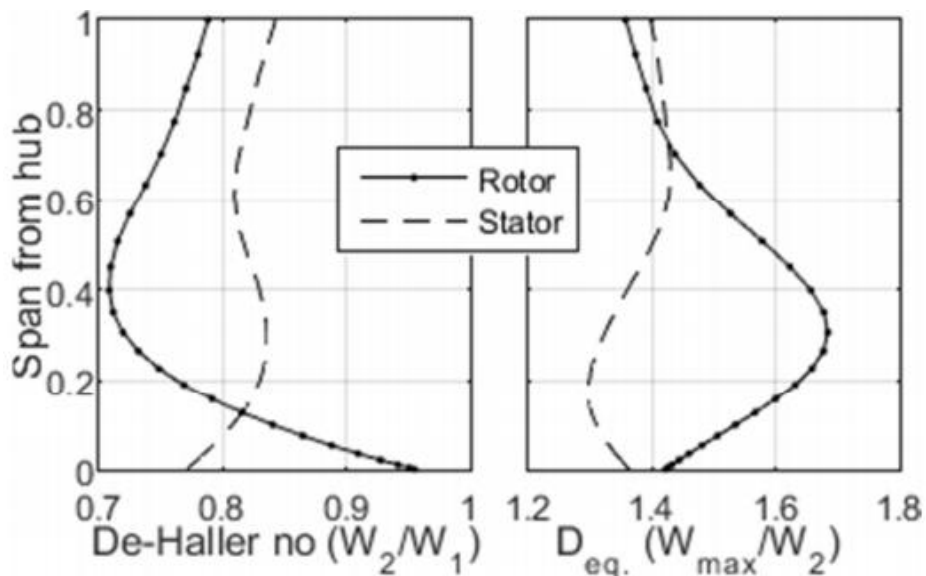


**Figure 2.6.** Spanwise distribution of equivalent diffusion factor and De-Haller number

In Figure 2.6, the rotor hub De-Haller number reaching 0.95 indicates reduced loading. This is the reason for the higher axial velocity at the hub and increased hub

diameter (from rotor LE to TE). In respect to De-Haller number, the stator hub is highly loaded within acceptable levels (>0.72). Besides, higher solidity makes the Equivalent Diffusion Factor suitable for both rotor and stator. The De-Haller number is as can be seen in Equation 2.3.

$$\text{De-Haller} = \frac{W_2}{W_1} \qquad (2.3)$$

and Equivalent Diffusion Factor is as can be seen in Equation 2.4.

$$D_{eq} = \frac{W_{max}}{W_2} \qquad (2.4)$$

# 3. HIGH FIDELITY AERODYNAMIC SIMULATION (CFD) METHODOLOGY

## 3.1 The Solver Theory and Utilized Software

In this study, ANSYS engineering simulation and 3D design software were used. Turbogrid was used to mesh the flowfield of the turbomachinery and CFX was used to compute the flowfield. Air is considered to be the ideal gas and the temperature depends on the viscosity, specific heat capacity, and conductivity. As can be seen in Equation 3.1, ideal gas equation is related to density with its absolute values of pressure and temperature;

$$\rho = \frac{P}{R_{air}T} \quad [\text{kg/m}_3]$$  (3.1)

As can be seen in Equation 3.2, instead of solving the original Navier-Stokes Equation for all the length and timescales of turbulence, which is far beyond the capability of current computers, time-varying velocities of any direction 'i' are decomposed into low frequency (mean) and high frequency (fluctuating) components such that:

$$V_i = V_i + v'_i$$  (3.2)

The Navier-Stokes equation requires very high computational capacity and takes into account the turbulence in the three-dimensional flow field in terms of all length and time. Reynolds-averaged Navier-Stokes (RANS) equations ( were used to solve the compressible flowfield by vertex centered finite volume method with CFX second-order upwind-biased scheme (Equation 3.3).

$$\frac{\partial \rho V_i}{\partial t} + \frac{\partial}{\partial x_j}(\rho V_i V_j) = -\frac{\partial P}{\partial x_i} + \frac{\partial}{\partial x_j}\left[\mu\left(\frac{\partial V_i}{\partial x_j} + \frac{\partial V_j}{\partial x_i}\right) - \rho \overline{v_i v_j}\right]$$  (3.3)

where the term $\rho\overline{v_i v_j}$ expresses Reynolds stresses and consider mixing on account of turbulent fluctuations [16]. The same arguments also apply to the energy equation that includes the turbulent mixing.

The mass continuity equation is unaltered with this separation process and can be written as can be seen in Equation 3.4.

$$\frac{\partial\rho}{\partial t}+\frac{\partial}{\partial x_j}(\rho V_j)=0 \tag{3.4}$$

Energy equation is given in Equation 3.5.

$$\frac{\partial\rho H}{\partial t}-\frac{\partial P}{\partial t}+\frac{\partial}{\partial x_j}(\rho V_j H)=\frac{\partial}{\partial x_j}(k\frac{\partial T}{\partial x_j}-\rho\overline{u_j h})+\frac{\partial}{\partial x_j}\left\{V_i\left[\mu\left(\frac{\partial V_i}{\partial x_j}+\frac{\partial V_j}{\partial x_i}\right)-\rho\overline{v_i v_j}\right]\right\} \tag{3.5}$$

Total enthalpy *H* in this equation now includes the contribution from turbulent kinetic energy. The term $\rho\overline{u_j h}$ takes into account the additional flux due to turbulence whereas the term containing Reynolds stresses considers viscous dissipation due to both mean and fluctuating velocity components [16].

For the closure of turbulent terms, the well-known Boussinesq turbulent viscosity assumption is used to model Reynolds stresses, where the molecular viscosity is replaced by an effective (molecular+turbulent) viscosity field to take into account the effects of turbulent fluctuations in an isotropic manner (Equation 3.6), that is;

$$-\rho\overline{v_i v_j}=\mu_{turbulent}\left(\frac{\partial V_i}{\partial x_j}+\frac{\partial V_j}{\partial x_i}\right) \tag{3.6}$$

And similarly, turbulent conductivity ($\mu turbulent/Prturbulent$) is defined as can be seen in Equation 3.7.

$$-\rho\overline{u_j h}=\frac{\mu_{turbulent}}{Pr_{turbulent}}\frac{\partial h}{\partial x_j} \tag{3.7}$$

Where $Pr_{turbulent}$ is the Prandtl number based on turbulent viscosity. The problem is now reduced to obtaining $\mu_{turbulent}$ as a function of space. Shear Stress Transport (SST) turbulence closure [16] is selected to model turbulent viscosity field, which is known to provide robust results in flowfields with adverse pressure gradients [17]. In this model, turbulent viscosity depends on the turbulent kinetic energy ($k$) and turbulent frequency ($\omega$) with a low- Reynolds number limiter as (Equation 3.8):

$$\mu_{turbulent} = \frac{\rho k}{\omega} \frac{1}{\max\left[\dfrac{1+\rho k/6\mu\omega}{0.024+\rho k/6\mu\omega}, \left(\dfrac{\partial V_i}{\partial x_j}+\dfrac{\partial V_j}{\partial x_i}\right)\dfrac{F_2}{0.62\omega}\right]} \tag{3.8}$$

Below partial differential equations are used as governing equations to k and $\omega$, respectively [16]. For the turbulent kinetic energy (k) (Equation 3.9);

$$\frac{\partial(\rho k)}{\partial t}+\frac{\partial}{\partial x_j}\left(\rho V_j k\right)=\frac{\partial}{\partial x_j}\left[\left(\mu+\frac{\mu_{turbulent}}{0.176F_1+1}\right)\frac{\partial k}{\partial x_j}\right]+P_k-0.09\rho k\omega \tag{3.9}$$

And for the specific dissipation ($\omega$) (Equation 3.10);

$$\frac{\partial\rho\omega}{\partial t}+\frac{\partial\left(\rho V_j\omega\right)}{\partial x_j}=\frac{\partial}{\partial x_j}\left[\left(\mu+\frac{\mu_{turbulent}}{0.8317757F_1+1.168224299}\right)\frac{\partial\omega}{\partial x_j}\right]$$
$$+(1-F_1)\frac{1.712\rho}{\omega}\frac{\partial k}{\partial x_j}\frac{\partial\omega}{\partial x_j}+\left(\frac{5}{9}F_1+0.44(1-F_1)\right)\frac{\omega}{k}P_k+\left(0.0828-0.0078F_1\right)\rho\omega^2 \tag{3.10}$$

Where *Pk* is a production of turbulence due to viscous forces and modeled as (Equation 3.11);

$$P_k=\mu_{turbulent}\left(\frac{\partial V_i}{\partial x_j}+\frac{\partial V_j}{\partial x_i}\right)\frac{\partial V_i}{\partial x_j}-\frac{2}{3}\frac{\partial V_k}{\partial x_k}\left(3\mu_{turbulent}\frac{\partial V_k}{\partial x_k}+\rho k\right) \tag{3.11}$$

Submodels to take into account laminar-to-turbulent transition (both intermittency and cross-flow) and small modifications in the reattachment regions are also applied for slight enhancements. Readers are referred to as reference [16] for further details about these submodels. In the above equations, *F₁* (Equation 3.12) and *F₂* (Equation 3.14) are blending functions, which have a value of '1' near the surfaces (y=0m) (Equation 3.13), and gradually reduces to '0' away from the walls (y>>0m)

(Equation 3.15), and defined as Where *Pk* is a production of turbulence due to viscous forces and modeled as;

$$F_1 = \tanh(\arg_1{}^4) \qquad (3.12)$$

$$\arg_1 = \min\left( \max\left( \frac{\sqrt{k}}{0.09\omega y}, \frac{500\mu}{\rho\omega^2 y^2} \right), \frac{3.424\rho k}{\max\left( \dfrac{1.712\rho}{\omega} \dfrac{\partial k}{\partial x_j} \dfrac{\partial \omega}{\partial x_j}, 10^{-10} \right) y^2} \right) \qquad (3.13)$$

$$F_2 = \tanh(\arg_2{}^2) \qquad (3.14)$$

$$\arg_2 = \max\left( \frac{2\sqrt{k}}{0.09\omega y}, \frac{500\mu}{\rho\omega y^2} \right) \qquad (3.15)$$

The vertex-centered finite volume method is employed to numerically solve the governing equations. For the interpolation of advection terms, CFX 'High-Resolution Scheme,' which is basically an upwind scheme with second order accuracy [16], is employed.

Below correlation (Sutherland's law) is used to model dynamic viscosity of air solely as a function of absolute temperature in the range (0<T<555 K) (Equation 3.16);

$$\mu = 1.716/10^5 \left( \frac{T}{273.15} \right)^{3/2} \frac{383.55}{T+110.4} \quad [\frac{kg}{ms}] \qquad (3.16)$$

For constant-pressure specific heat capacity (*cp*) of air, pressure dependence is neglected and the below polynomial is used in the range 100-1000K (Equation 3.17):

$$c_p = (1161.482) - (2.368819)T + (0.01485511)T^2 - (5.034909/10^5)T^3 + (9.928569/10^8)T^4$$
$$-(1.111097/10^{10})T^5 + (6.540196/10^{14})T^6 - (1.573588/10^{17})T^7 \quad [J/kgK] \qquad (3.17)$$

Enthalpy change (Equation 3.18), specific heat capacity at constant volume (cv) (Equation 3.19) and internal energy (e) change (Equation 3.20) are expressed as below, respectively:

$$h - h_{ref} = \int_{T_{ref}}^{T} c_p(T)dT \qquad (3.18)$$

19

$$c_v(T) = c_p(T) - R_{air} \tag{3.19}$$

$$e - e_{ref} = \int_{T_{ref}}^{T} c_v(T)dT \tag{3.20}$$

Finally, the change in entropy is calculated by (Equation 3.21):

$$s - s_{ref} = \int_{T_{ref}}^{T} \frac{c_p(T)}{T}dT - R_{air}\ln(\frac{P}{P_{ref}}) \tag{3.21}$$

For advance turbulent control, reattachment modifications and are used to model turbulent viscosity field. SST sub-models were selected in the transition from laminar to turbulent. These are Intermittency Model and Cross Flow Transition. The k-ω-based shear stress transport (SST) models make near-wall treatments in low-Reynolds number calculations. This is because accurate results are obtained in the solution of flow fields with adverse pressure gradients.

## 3.2 Validation Rotor 37

### 3.2.1 Mesh Independency

Verification of the simulation for the new fan to be designed is very important. So we used NASA Rotor 37, which has its experiments in the literature, for the verification study.

A mesh independence study was performed for the NASA rotor 37. Firstly, the geometry is divided into a coarse, medium and fine mesh. Then fine_v2 mesh was created. In this fine_v2 mesh, the meshes in the passage and inlet-outlet were the same as medium mesh. But, first layer thickness was decreased and the meshes in the blade to blade and tip gap were increased in order to obtain more accurate results especially in the rotor tip zone. The tip gap is 0.4 mm at 100% Speedline and 17188.7 angular velocity. Different mesh sizes for NASA Rotor 37 are given in Table 3.1. Pressure ratio and efficiency at %100 speedline in different mesh sizes are given in Table 3.2.

**Table 3.1.** Different Mesh Size For Rotor 37

| | Number of elements | First layer thickness (m) | Hub to tip | | Blade to blade | | Tip gap | Inlet-Outlet |
|---|---|---|---|---|---|---|---|---|
| | | | Number of elements | Maximum expansion rate | Global size factor | Maximum expansion rate | Number of elements | Number of streamwise elements |
| Coarse | 0,85 x 10^6 | 4 x 10^-6 | 40 | 1,42 | 1,5 | 1,3 | 20 | 24 |
| Medium | 3,40 x 10^6 | 3 x 10^-6 | 100 | 1,17 | 2 | 1,3 | 35 | 42 |
| Fine | 8,50 x 10^6 | 2 x 10^-6 | 160 | 1,097 | 2,5 | 1,3 | 50 | 60 |
| Fine-2 | 14,40 x 10^6 | 1 x 10^-6 | 100 | 1,17 | 4 | 1,3 | 60 | 42 |

**Table 3.2.** Pressure ratio and Efficiency at %100 speedline (17188.7 r/min angular velocity)

| | Total to total (Overall) | |
|---|---|---|
| | Pressure ratio | Efficiency |
| Coarse | 2,05 | 0,85 |
| Medium | 2,08 | 0,86 |
| Fine | 2,08 | 0,86 |
| Fine-2 | 2,08 | 0,86 |

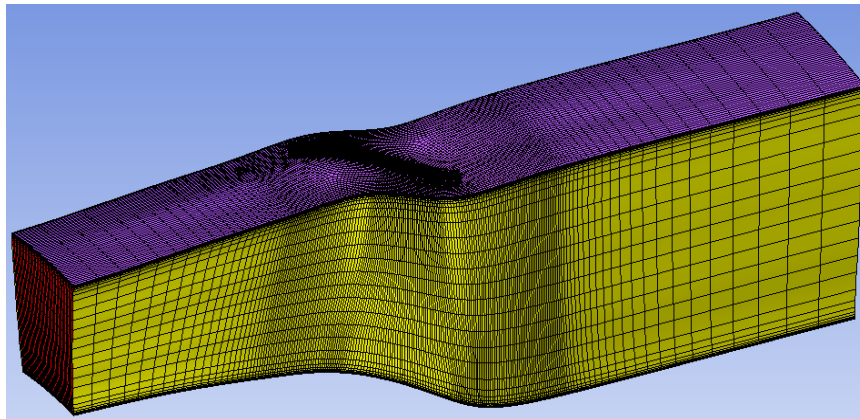The mesh structure on the geometry given for coarse mesh size is shown in Figure 3.1.



**Figure 3.1.** Coarse Mesh Size

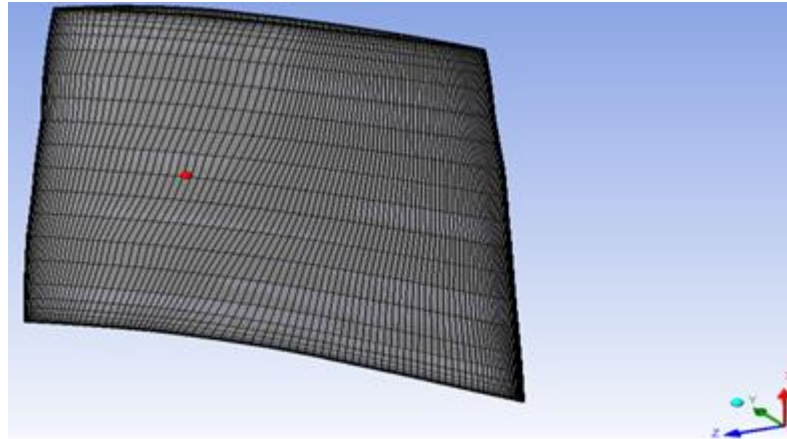The mesh structure on the blade given for coarse mesh size is shown in Figure 3.2.



**Figure 3.2.** Coarse Mesh Size on Blade

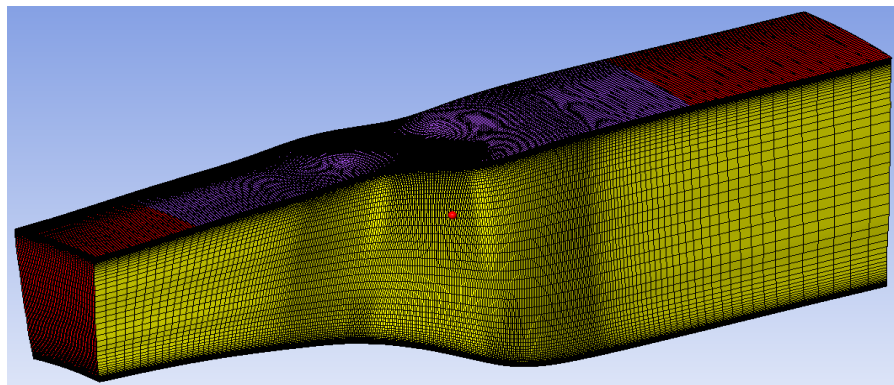The mesh structure on the geometry given for medium mesh size is shown in Figure 3.3.



**Figure 3.3.** Medium Mesh Size

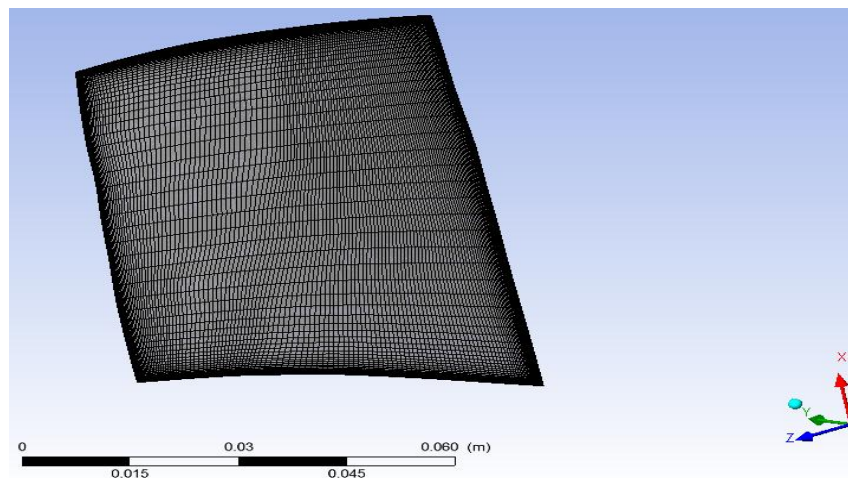The mesh structure on the blade given for medium mesh size is shown in Figure 3.4.



**Figure 3.4.** Medium Mesh Size on Blade

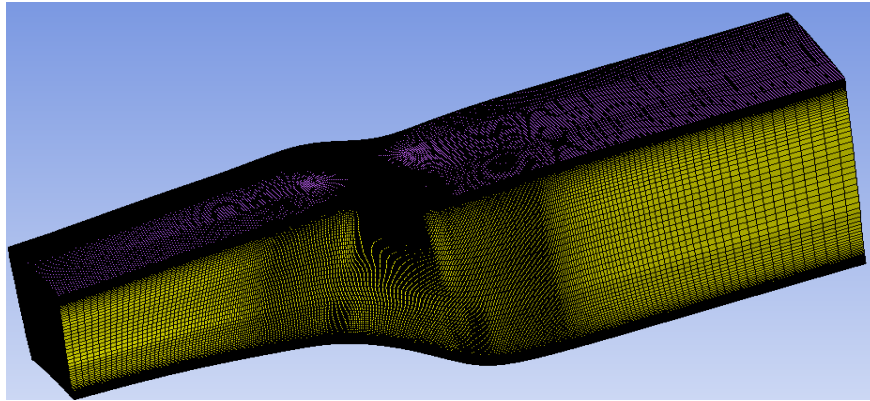The mesh structure on the geometry given for fine mesh size is shown in Figure 3.5.



**Figure 3.5.** Fine Mesh Size

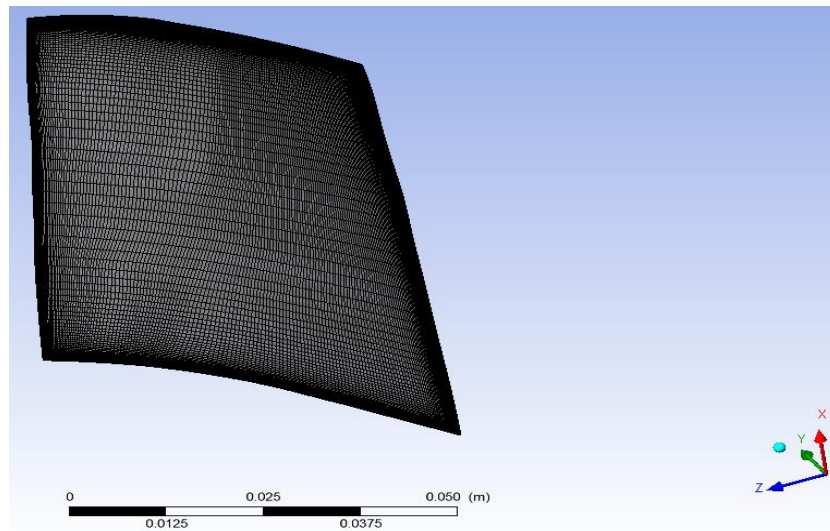The mesh structure on the blade given for fine mesh size is shown in Figure 3.6.



**Figure 3.6.** Fine Mesh Size on Blade

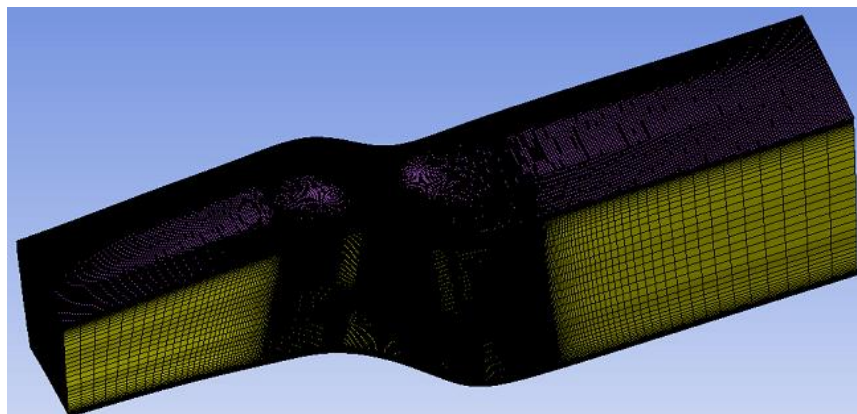The mesh structure on the geometry given for fine_v2 mesh size is shown in Figure 3.7.



**Figure 3.7.** Fine_v2 Mesh Size

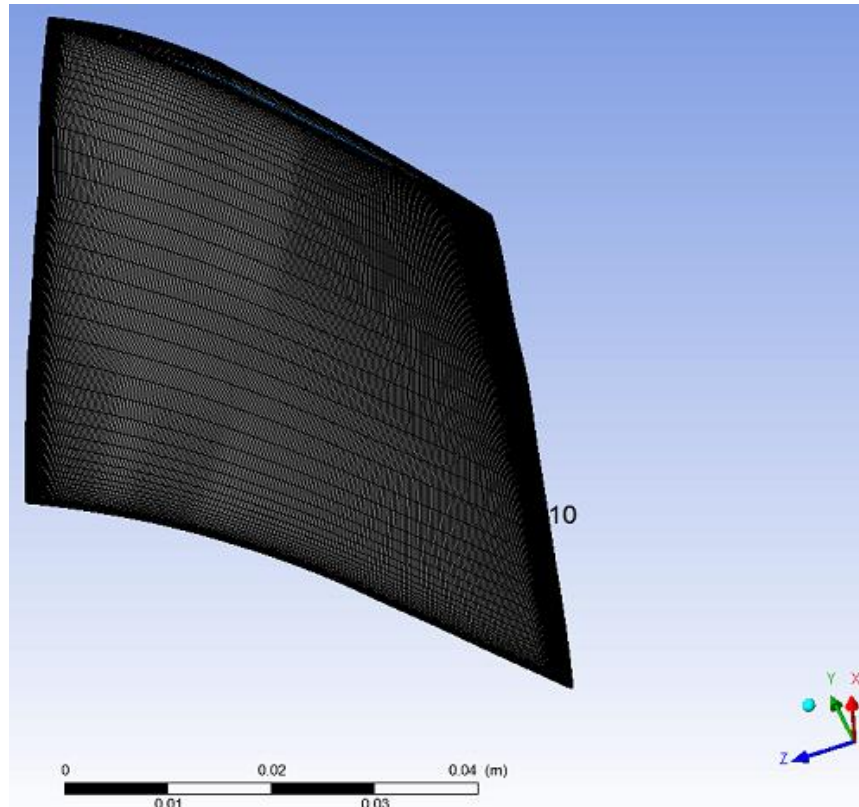The mesh structure on the blade given for fine_v2 mesh size is shown in Figure 3.8.



**Figure 3.8.** Fine_v2 Mesh Size on Blade

## 3.2.2 Fluid Flow Simulation

CFX was used for the fluid solution. Since the pressure and temperature from the hub to the shroud are different values, the pressure and temperature profiles were entered at the inlet. The output pressure was input to provide the desired mass flow rate at the outlet. Radial equilibrium pressure averaging was used at exit. The settings used in fluid models are given in Table 3.3. The effect of these settings on the solution was examined separately. The transitional turbulence model and reattachment modification are important. We will use turbulence and advanced turbulence control settings in Table 3.3 in the simulation of the new fan to be designed. The solution in which these Advance Turbulence Control options, Wall Function and Intermittency Model were not used was given as SST(default) in Figures 3.9 and 3.10. As understood in Figures 3.9 and 3.10, the options used in this turbulence and advanced turbulence control significantly improved the validation of the mesh.

**Table 3.3.** Fluid Models Settings

| Turbulence | Advance Turbulence Control |
|---|---|
| SST | Compressible Production |
| Wall Function | Curvature Correction |
| Transitional  Turbulence | Reattachment Modification |
| Intermittency Model | |
| Cross Flow Transition | |

In these settings, coarse, medium, fine and fine_v2 meshes were solved at 100% speedline and 17188.7 angular velocity. As understood in Figure 3.9 and Figure 3.10, the result of medium mesh and fine mesh were very close to each other. For this reason, medium mesh was used instead of fine mesh. The medium mesh is sufficient. Although the coarse mesh was very rough, a coarse mesh could be used with some improvement.
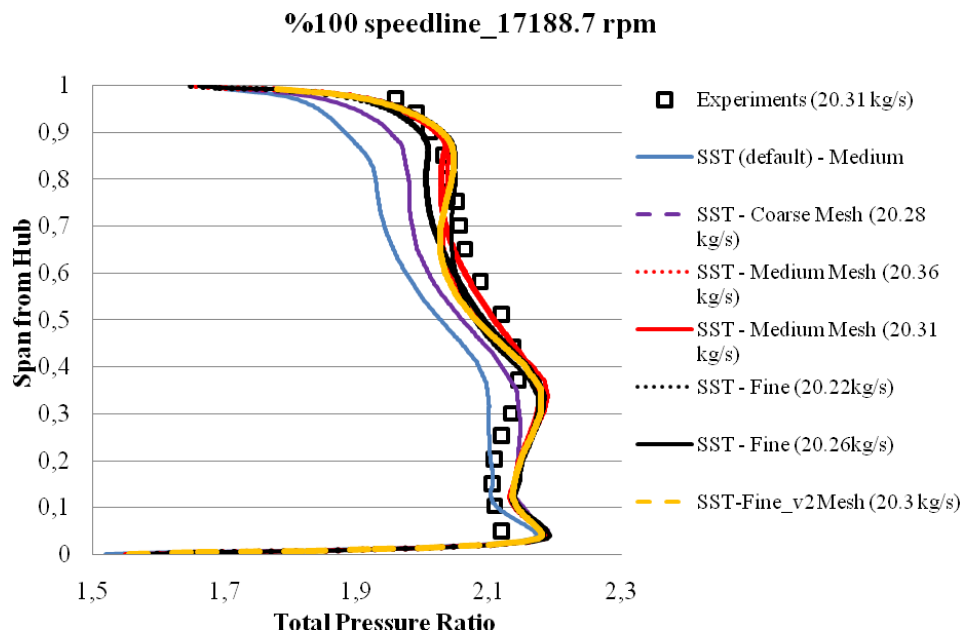


**Figure 3.9.** Total Pressure Ratio For Different Mesh Sizes(SST)

**%100 speedline _17188.7 rpm**

Legend:
□ Experiments (20.31 kg/s)
— SST (default) - Medium Mesh
- - SST - Coarse Mesh (20.28 kg/s)
⋯ SST - Medium Mesh (20.36 kg/s)
— SST - Medium Mesh (20.31 kg/s)
⋯ SST - Fine Mesh (20.22 kg/s)
— SST - Fine Mesh (20.26 kg/s)
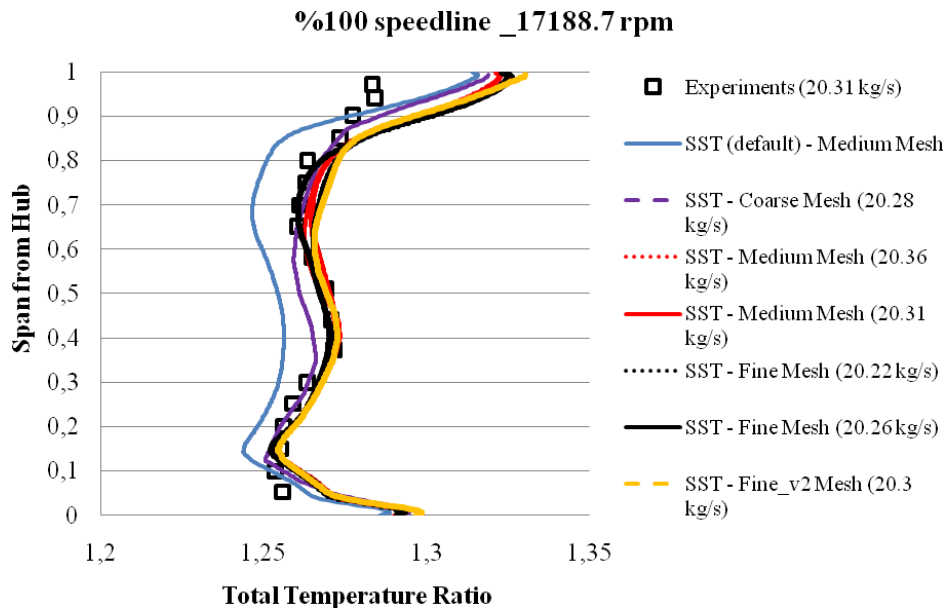- - SST - Fine_v2 Mesh (20.3 kg/s)

**Figure 3.10.** Temperature Ratio For Different Mesh Sizes(SST)

Relative Mach number at %10, %50, %95 spans are shown as a result of the solution made with medium, coarse and fine mesh in Figure 3.11, Figure 3.12, Figure 3.13. The area where the shock occurred was not changed with mesh size. The shock seems to be wider due to coarse mesh. The medium mesh seems to be sufficient for solution.
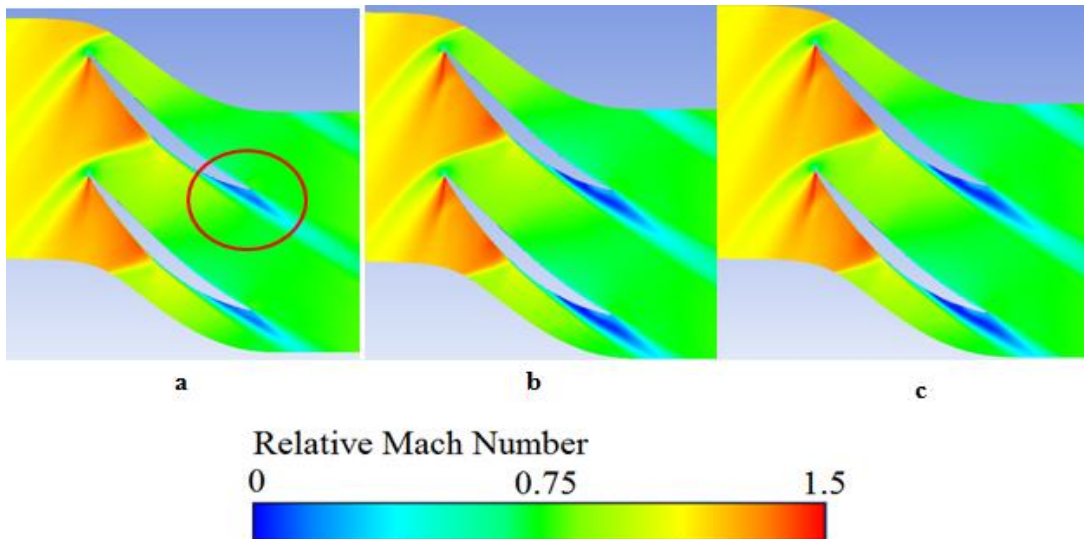


**Figure 3.11.** a) Coarse (20.28 kg/s), b) Medium (20.31kg/s), c) Fine (20.26 kg/s) 10% Span Mach  Number at 100% speedline -17188.7 rpm
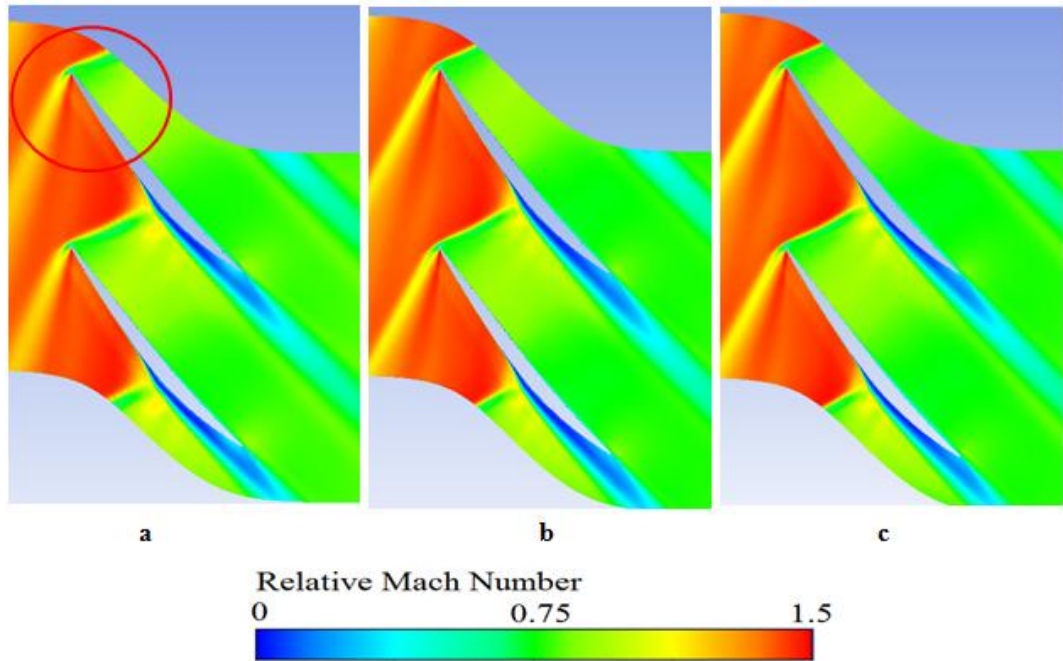
**Figure 3.12.** a) Coarse (20.28 kg/s), b) Medium (20.31kg/s), c) Fine (20.26 kg/s) 50% Span Mach Number at 100% speedline -17188.7 rpm
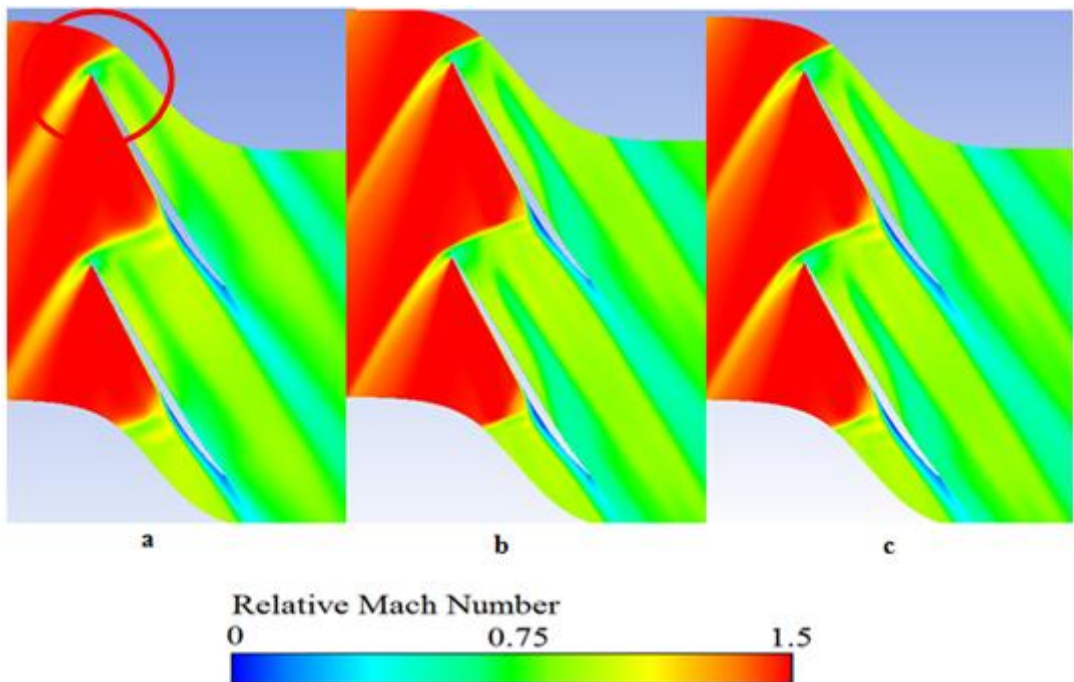


**Figure 3.13.** a) Coarse (20.28 kg/s), b) Medium (20.31kg/s), c) Fine (20.26 kg/s) 95% Span Mach Number at 100% speedline -17188.7 rpm

CFD results and experimental results were not consistent in tip region. In order for the CFD result to be compatible with the experimental result in the tip region, firstly fine_v2 mesh was created and examined the flow in this region. But, the results of

fine_v2 mesh is the same result of medium mesh. Secondly, the tip gap was arranged to 0.356 mm as in the AGARD report instead of 0.4 mm which is safety value and the solution was investigated. CFD results and experimental results were again inconsistent in the tip region.

Thirdly, solutions were made using different turbulence models. Fully Turbulent-Reynold Stress Model (RSM), Transition-Reynold Stress Model (EARSM-Explicit Algebraic Reynold Stress Model), RNG-k Epsilon models were used instead of SST (Shear Stress Transport). Finally, Gamma theta model was used instead of Intermittency Model. As understood in Figure 3.14 and Figure 3.15, CFD solutions made using different turbulence model did not change mismatch with the experiment in the tip region.

The inconsistent in tip region was seen in all previous CFD solutions. As stated in the Agard report, all turbulence models can not predict the strong flow deceleration in the outer wall boundary layer, and the high loss seems to appear as a consequence of the interaction between the passage shock and the leakage flow "vortex".
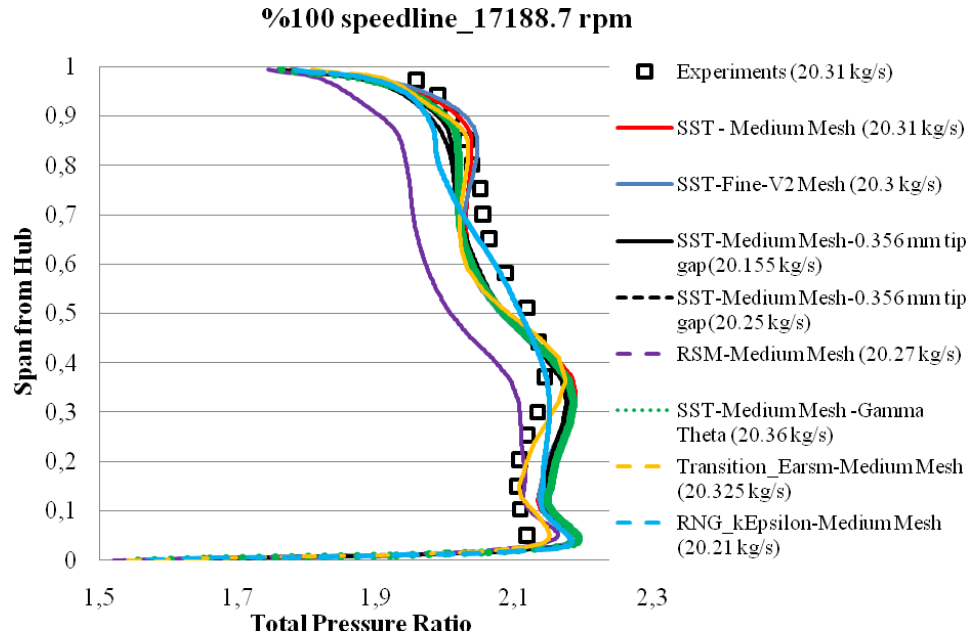


**Figure 3.14.** Total Pressure Ratio For Different Tip Clearance Value And Turbulence Models
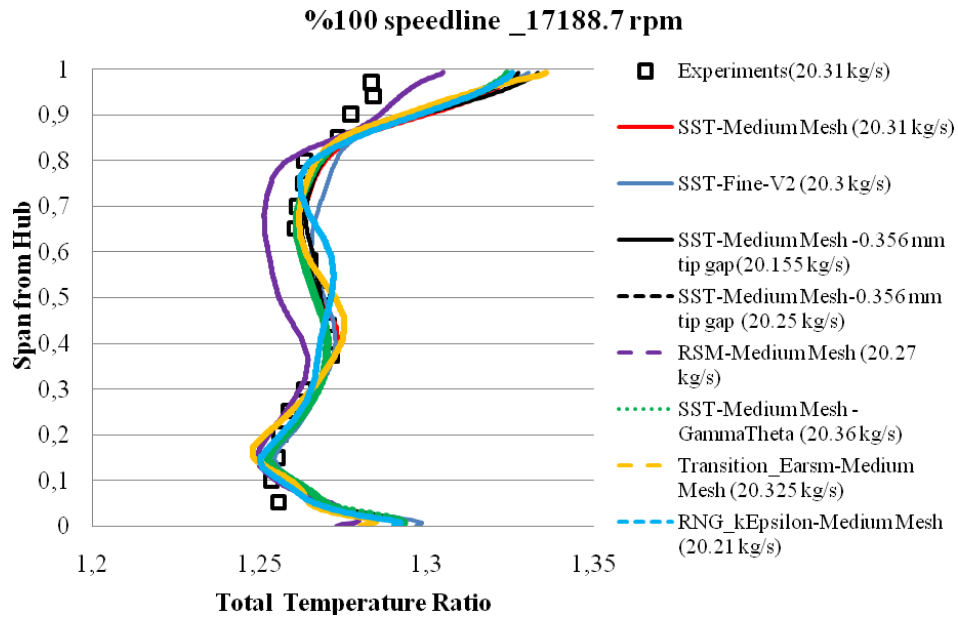
**Figure 3.15.** Total Temperature Ratio For Different Tip Clearance Value And Turbulence Models

The well-known Shear Stress Transport (SST) model was used for the turbulence closure for the Reynolds-Averaged Navier-Stokes Equations (RANS). This model is known to be accurate in boundary layers of flows with adverse pressure gradients, as strongly encountered in fans and compressors. It was observed during preliminary test-CFD comparisons that laminar-turbulence transition modelling is very critical for the accurate hub to tip distributions. Therefore, intermittency transition and cross-flow transition models were activated within the SST model. In addition, reattachment modification option available in the CFX solver was found to be beneficial towards better accuracy. Also, compressible production and curvature correction modifications, although not found to make notable changes, were activated.

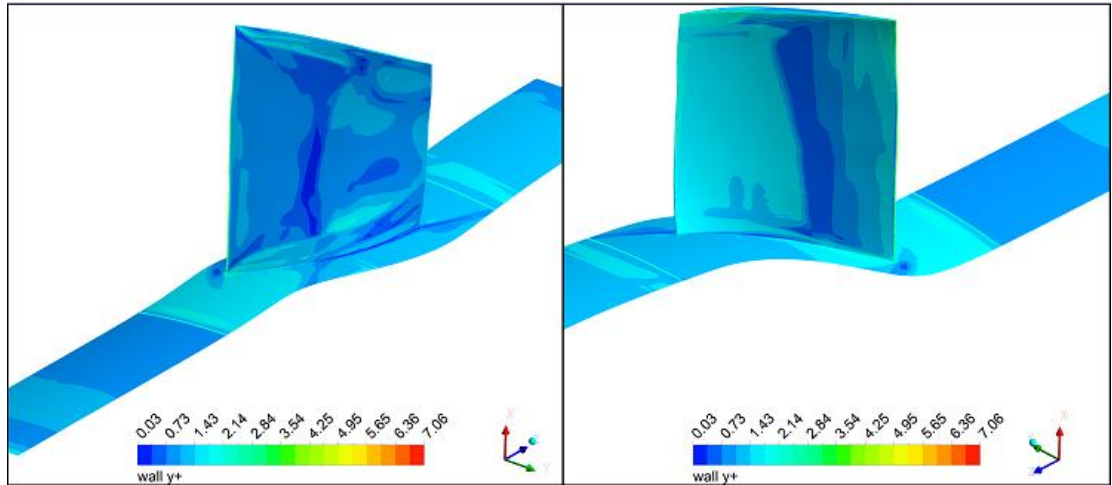Yplus contours for NASA Rotor 37 are shown in Figure 3.16. Yplus must be lower than 5.

**Figure 3.16.** Yplus contours for NASA Rotor 37

# 4. SIMULATION OF THE DESIGNED FAN

## 4.1. Simulation of the Original Fan

The solidity at the stator hub is already high. At the stator hub loading and the Mach number is high. The effect of wake mixing should be taken into account as a result of these effects. More solidity is required to reduce loading. Also, the hub loading can be reduced to decrease mixing losses. Three-dimensional design features (i.e. bow lean and sweep) can reduce hub loading. Another way to increase solidity is to increase the number of stator blades. However, increasing the number of stator blades is unsatisfactory in terms of production. Because it is unsuitable in terms of production if the pitch distance falls below 2 cm. Moreover, it is not desirable that the solidity of the mid and tip sections is high. Because the loading in the regions is not high. Therefore, it can be modified to increase the hub solidity locally and to reduce the tip solidity locally.

Streamwise total pressure distribution at between rotor and stator are shown in Figure 4.1.
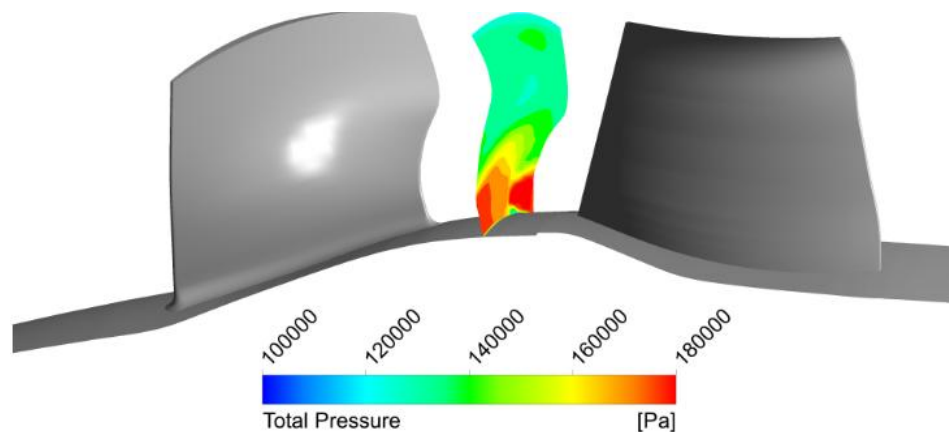


**Figure 4.1.** Streamwise total pressure distribution at between Rotor and Stator
Total Pressure contours at 0.1, 0.5 and 0.9 spans for the rotor are shown in Figure 4.2. The rotor hub is the most loaded section.
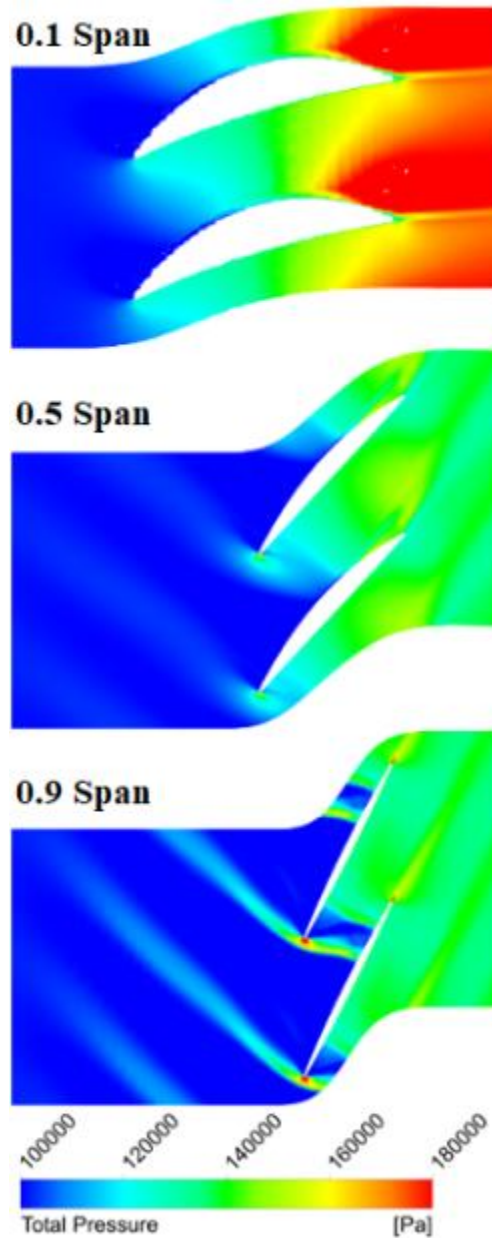
**Figure 4.2.** Total Pressure contours at 0.1, 0.5 and 0.9 spans for Rotor

Ma number chordwise distribution for rotor at the 0.9 (top), 0.5 (mid), and 0.1 (bottom) spans is shown Figure 4.3. Ma number does not increase because solidity is high and radius is high in the hub region. LE spikes occur at 0.5 and 0.9 spans. More than one shock occurs at 0.9 spans.
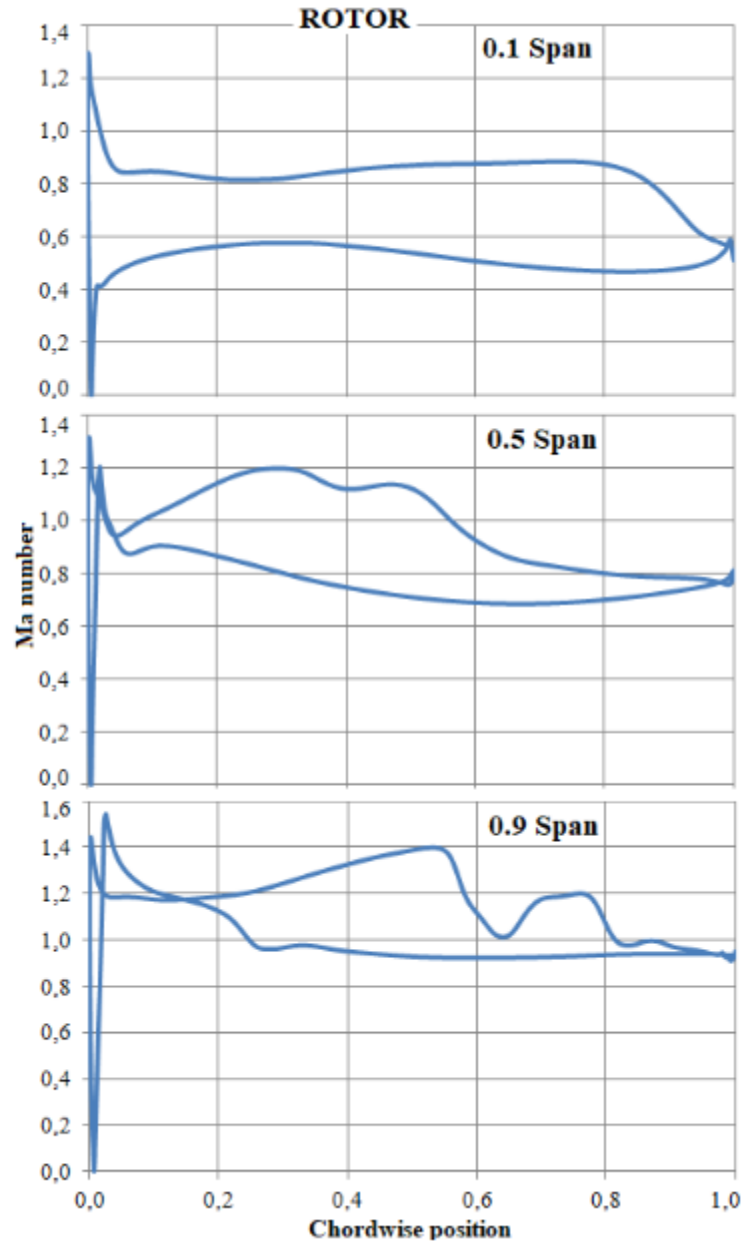
**Figure 4.3.** Ma number chordwise distribution for rotor at the 0.9 (top), 0.5 (mid), and 0.1 (bottom) spans.

Relative Mach contours at 0.1, 0.5 and 0.9 spans for the rotor are shown in Figure 4.4. LE spikes occur at 0.5 and 0.9 spans. More than one shock occurs at 0.9 spans.
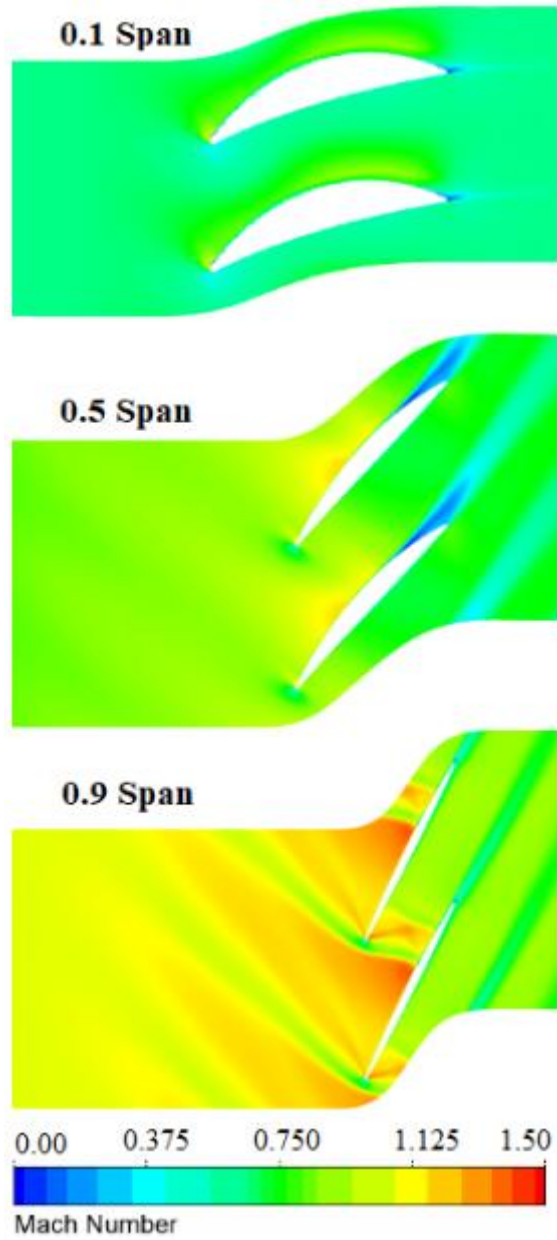
**Figure 4.4.** Relative Mach contours at 0.1, 0.5 and 0.9 spans for Rotor

Yplus contours for Rotor and Stator are shown in Figure 4.5. As shown in the figure, Yplus is smaller than 5.
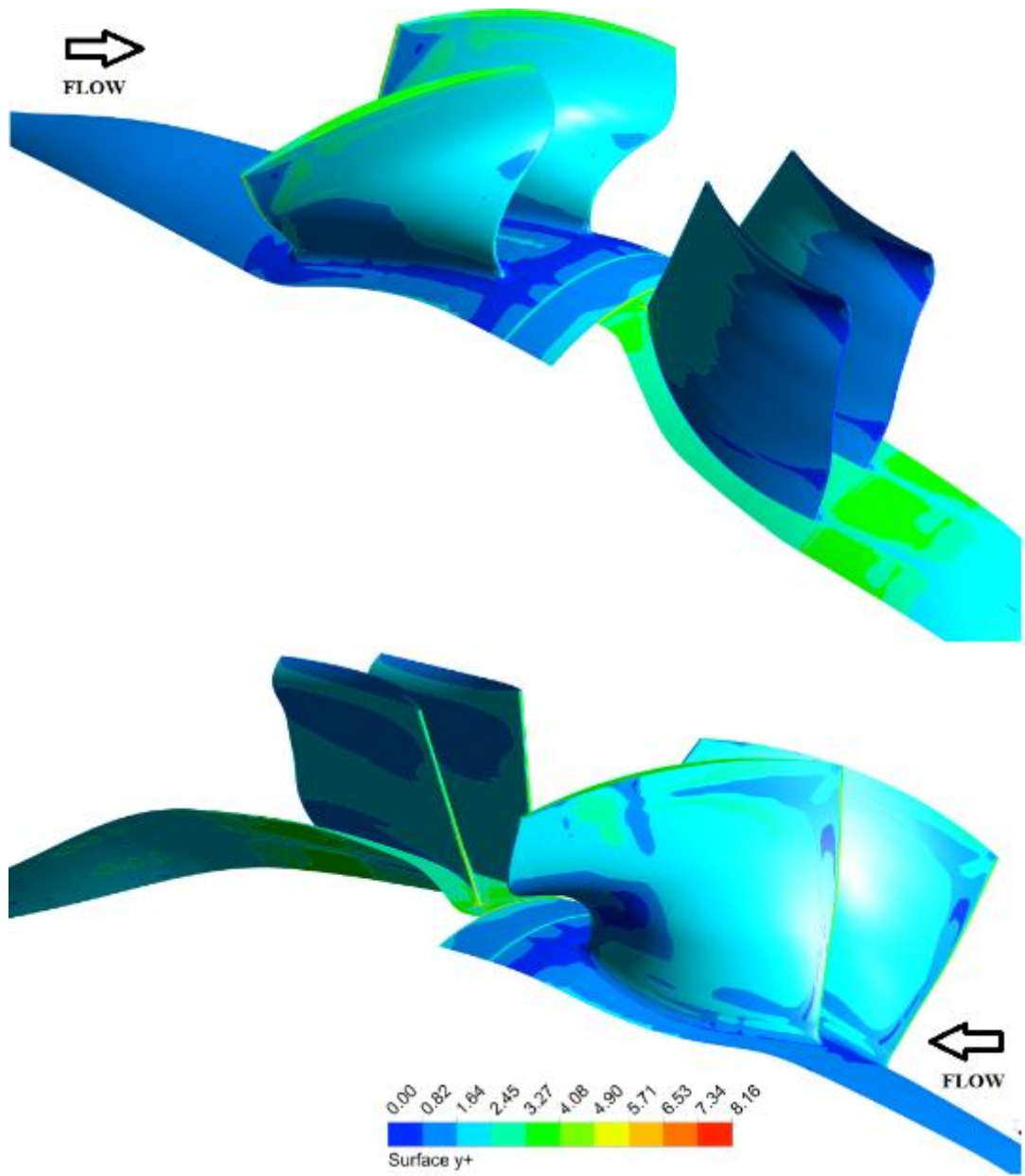
**Figure 4.5.** Yplus contours for Rotor and Stator

Streamwise entropy distribution at between Rotor and Stator are shown in Figure 4.6.
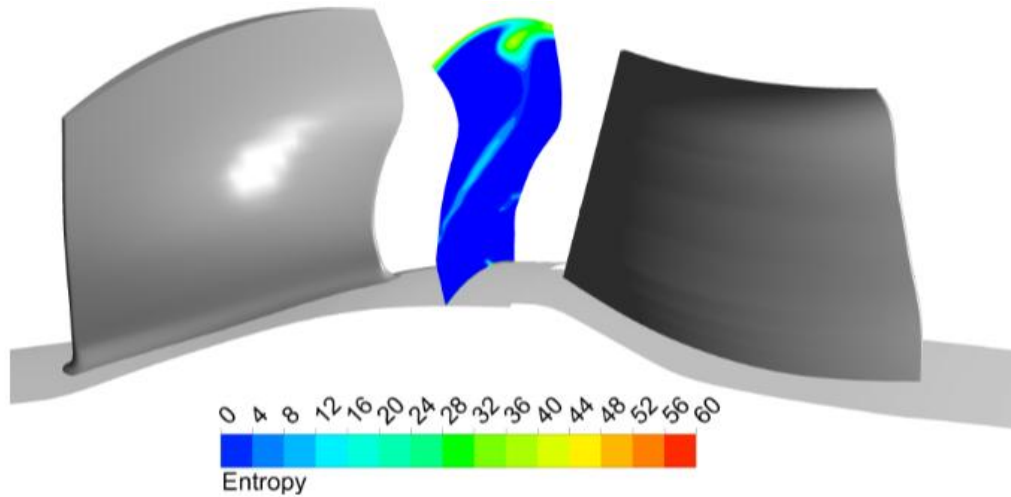
**Figure 4.6.** Streamwise entropy distribution at between Rotor and Stator

Entropy contours at 0.1, 0.5 and 0.9 spans for the rotor are shown in Figure 4.7. There is a very strong wake zone at a 0.5 span. Entropy is high at a 0.9 span because tip leakage and shock occur. Thanks to the fillet and acceleration and without shock, entropy is low at the hub.
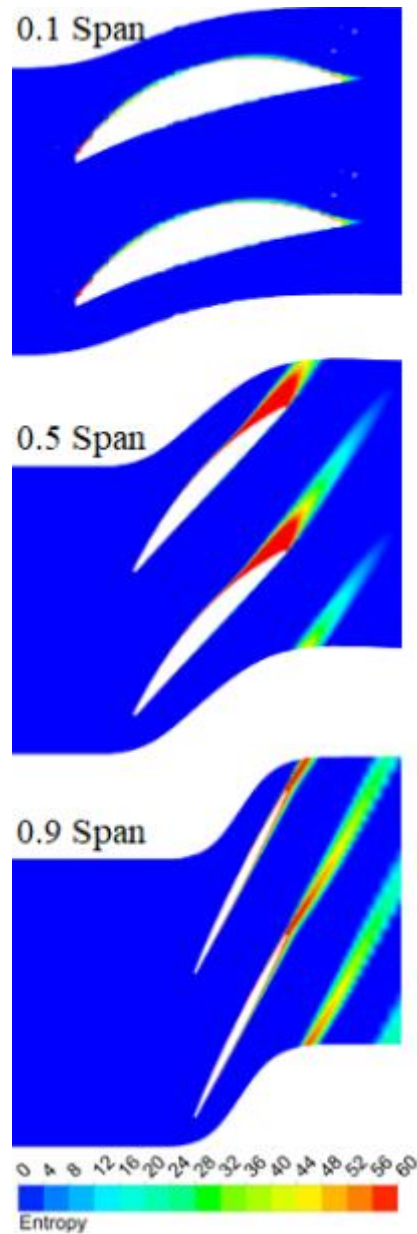
**Figure 4.7.** Entropy contours at 0.1, 0.5 and 0.9 spans for Rotor

## 4.2. Different Stator Configurations

Different cases are examined for stator solidity. Case A is the original stator geometry. In this case stator solidity(chord/pitch) is 3. In case B, the stator was linearly increased to hub solidity of 4.5. Case C, the hub still has high solidity and the tip solidity has been reduced by 20%. In addition, to reduce hub loading, aft-sweep and bow lean were employed. In Figure 4.8, sweep and lean are shown. Case D is like case B( no lean), but it has high solidity from hub to midsection and tip solidity is 20% less.

**Figure 4.8.** Different Stator Configurations Investigated. (a) Case A,
(b) Case B, (c) Case C (d) Case D

CFD results of the investigated stator configurations were examined. To calculate the total pressure ratio and the total isentropic efficiency for the four stator configurations examined, the inlet is taken as half-chord upstream of the rotor and three different outlet positions are compared:
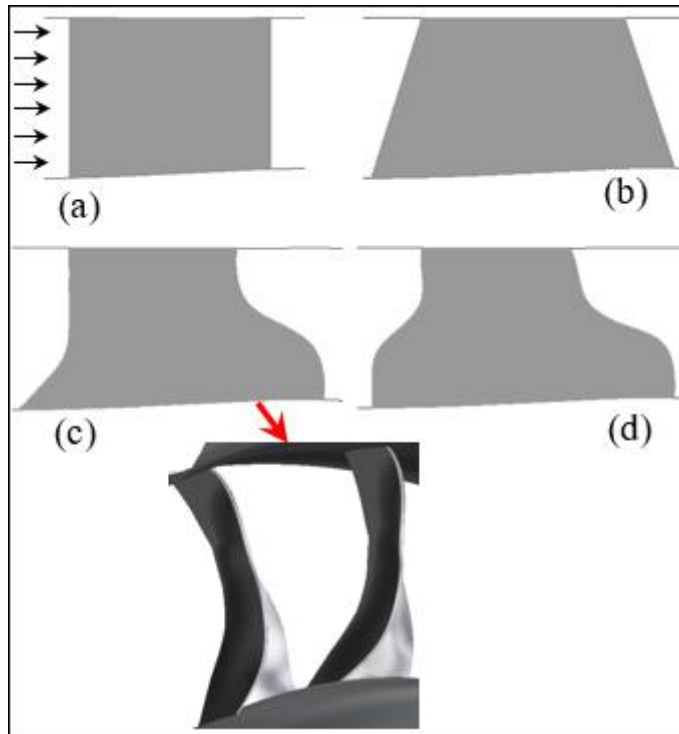
- First, the stator trailing edge takes as the outlet. There is no mixing loss.
- The second one takes half-chords downstream as the outlet. There is some amount of mixing loss.
- The third one three chord downstream are taken as the outlet. All mixing losses are included.

When mixing losses are not taken into account in the hub region, hub efficiency value is approximately %87 for all stator cases. The bypass stream efficiency is about %83. Shock losses are high in the rotor tip region. Targeted pressure ratios were obtained. Isentropic efficiency and pressure ratios calculated according to different outlet positions are given in Table 4.1. As shown in the table, as it moves downstream of trailing edge, the performance of the core stream is impaired and the performance of the bypass stream is not affected. In the case of B, the hub solidity is

higher than Case A. High solidity improves its core performance. But the linear taper causes the bypass performance to deteriorate. Case C, including sweep and bow lean, does not improve hub stream performance. In order to investigate the effect of lean, the cases with different amounts of lean were examined and it was observed that there was no adequate effect on the performance. Therefore, bow lean and sweep were not applied. Case C, tip solidity is less and this leads to increase bypass performance slightly. Therefore, Case D has smaller tip solidity, as in Case C. Thus, the performance of the bypass stream is improved. Case D, the performance of the core and bypass stream is high. Therefore it is chosen as the final design.

**Table 4.1.** Detailed Overall Performances For The Investigated Stator Configurations

| CASE A (ORIGINAL STATOR) | | $\Pi_{total}$ | $\eta$isent (%) |
|---|---|---|---|
| Stator Trailing Edge | Core | 1.60 | 87.4 |
| | Bypass | 1.39 | 83.1 |
| Half Stator Chord Down | Core | 1.56 | 84.7 |
| | Bypass | 1.39 | 82.9 |
| Three Stator Chords Down | Core | 1.51 | 79.1 |
| | Bypass | 1.38 | 80.4 |
| CASE B | | $\Pi_{total}$ | $\eta$isent (%) |
| Stator Trailing Edge | Core | 1.60 | 87.1 |
| | Bypass | 1.38 | 82.6 |
| Half Stator Chord Down | Core | 1.58 | 85.8 |
| | Bypass | 1.38 | 82.2 |
| Three Stator Chords Down | Core | 1.54 | 80.3 |
| | Bypass | 1.37 | 79.6 |
| CASE C | | $\Pi_{total}$ | $\eta$isent (%) |
| Stator Trailing Edge | Core | 1.60 | 87.3 |
| | Bypass | 1.39 | 83.5 |
| Half Stator Chord Down | Core | 1.58 | 85.7 |
| | Bypass | 1.39 | 83.0 |
| Three Stator Chords Down | Core | 1.53 | 79.6 |
| | Bypass | 1.38 | 80.5 |
| CASE D | | $\Pi_{total}$ | $\eta$isent (%) |
| Stator Trailing Edge | Core | 1.60 | 86.9 |
| | Bypass | 1.39 | 83.1 |
| Half Stator Chord Down | Core | 1.58 | 85.4 |
| | Bypass | 1.39 | 82.7 |
| Three Stator Chords Down | Core | 1.54 | 80.2 |
| | Bypass | 1.38 | 80.3 |

Three-dimensional geometry of the low pressure compression system with Case D stator is presented in Figure 4.9. The compressor design is the same as the original design except for the new stator (Case D). For the compressor in the final design, the pressure ratio for the rotor and stage(rotor+stator) is compared according to the results of the through-flow and CFD (Figure 4.10).
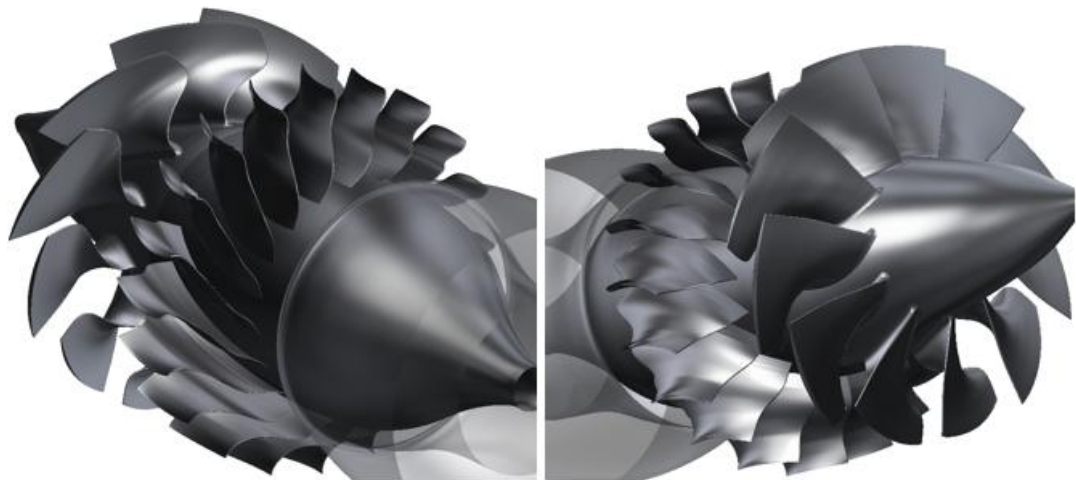
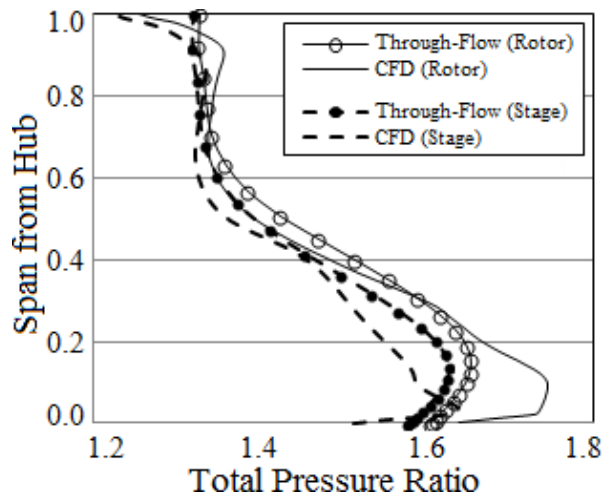**Figure 4.9.** Geometry with the wide-chord Case D Stator



**Figure 4.10.** Comparison Of Target (Through-Flow) And Achieved (Cfd) Pressure Ratio Distributions

For the stage (rotor + stator), the relative Mach number contours were examined near the hub(10%), mid-span(50%) and near tip(95%) spanwise cross-sections. At the near the hub (10%), although the rotor is very thickness there is no separation. In the stator, even if the incidence is small, local acceleration exists at the leading edge. With these corrections, local accelerations could not be eliminated. This is thought to be a result of the circular leading edge. Although the stator hub region is very loaded, there is no big separation. Even if no reverse flow occurs, a large low momentum region is formed which causes very large downstream mixing losses. This low momentum region is only slightly reduced in case D. Mean line (50% span) flow has no major problems. Two acceleration zones are formed on the rotor suction surface. It is thought that these acceleration zones will not have a big effect on flow. The flow

has a chocked double shock structure at the tip of the rotor. This is as intended in the design phase. Some flow separations at the stator tip occur due to tip leakage. And this flow separation may not be wholly eliminated.

Ma number chordwise distribution for case A, case B, case C, and case D at the 0.1, 0.5, 0.9 spans are shown in Figure 4.11. For Case B, the thickness between the pressure side (PS) and the suction side (SS) at 0.9 spans decreased. Solidity is high because the chord is long at the tip. Therefore friction losses are also high.
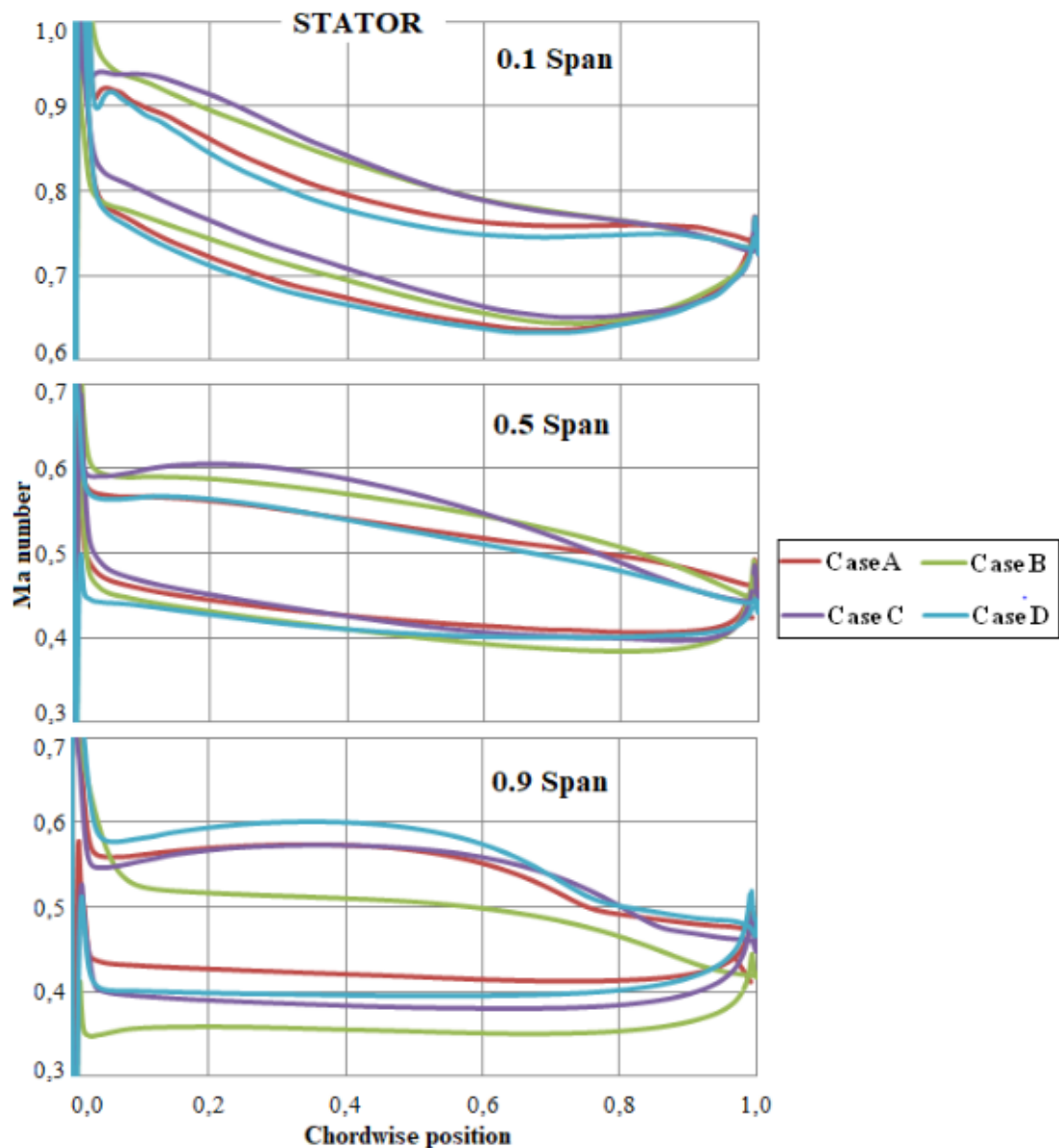


**Figure 4.11.** Ma number chordwise distribution for case A, case B, case C, and case D at the 0.9 (top), 0.5 (mid), and 0.1 (bottom) spans.

Comparison Relative Mach contours at 0.1, 0.5 and 0.9 spans for Case A Case B, Case C, and Case D are shown in Figure 4.12.
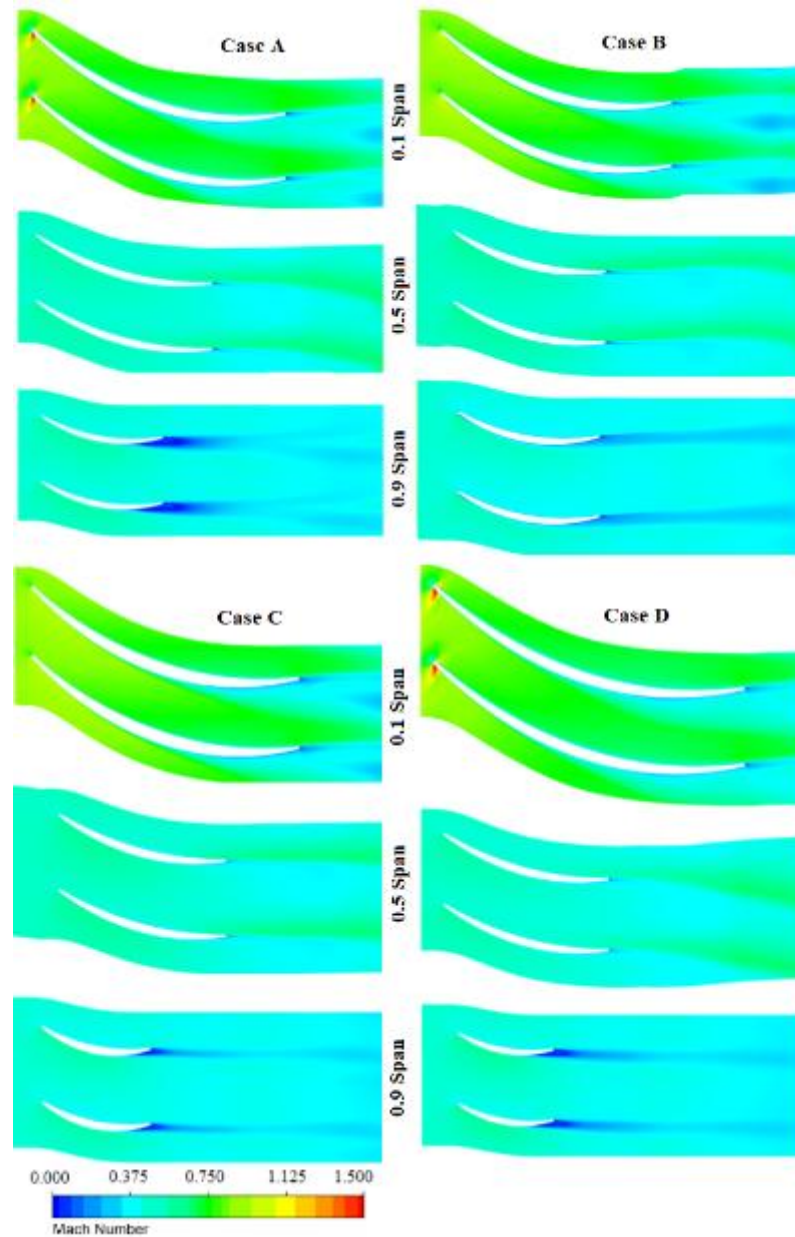


**Figure 4.12.** Comparison Relative Mach contours at 0.1, 0.5 and 0.9 spans for Case A Case B, Case C, and Case D

Streamwise total pressure distribution for Case A, Case B, Case C, and CaseD are shown in Figure 4.13. All cases look similar. The stator effect seems to be limited.
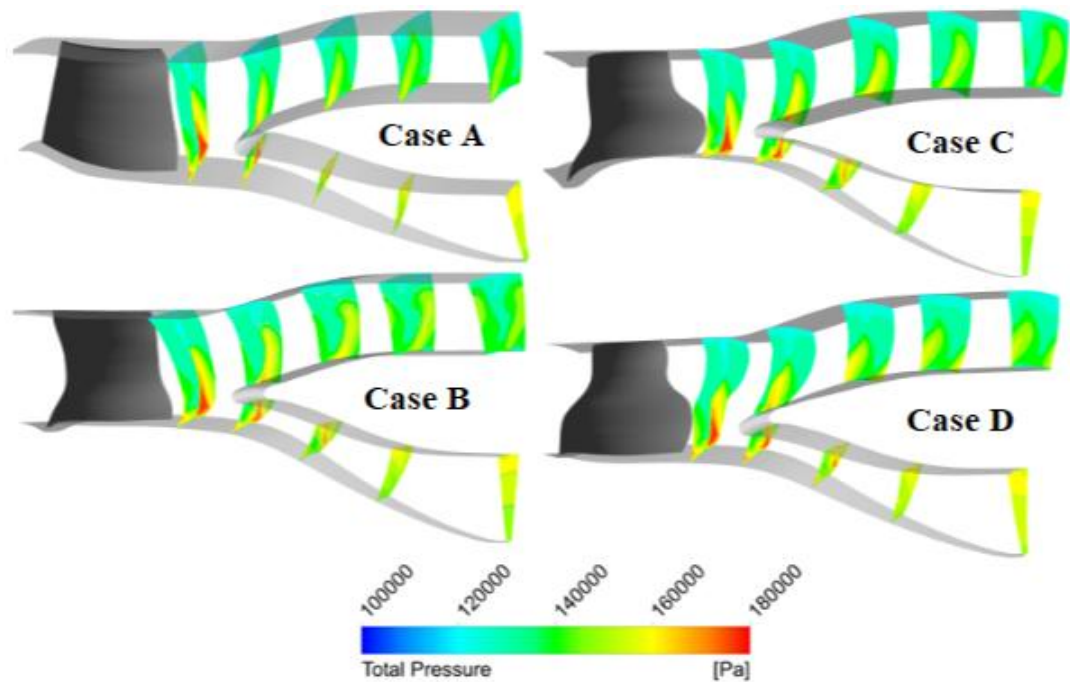
**Figure 4.13.** Streamwise total pressure distribution for Case A, Case B, Case C, and Case D

Streamwise entropy distribution for Case A, Case B, Case C, and Case D are shown in Figure 4.14. Wake shapes are different. Entropy is high at the tip due to tip leakage.
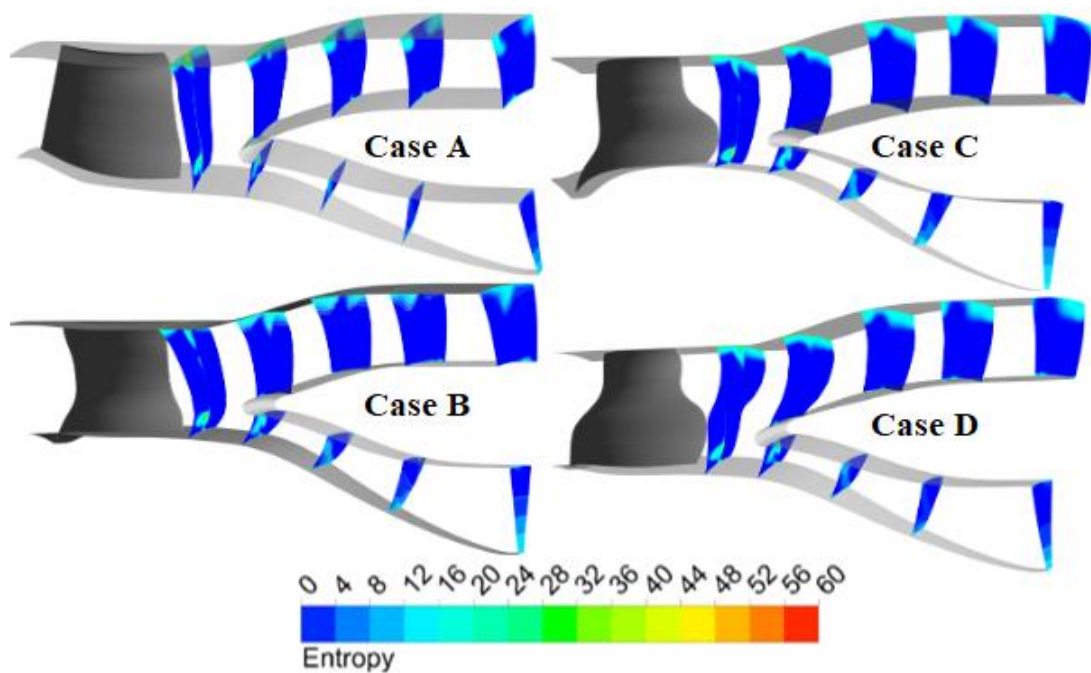


**Figure 4.14.** Streamwise entropy distribution for Case A, Case B, Case C, and Case D

Total Pressure contours at 0.1, 0.5 and 0.9 spans for all cases are shown in Figure 4.15. There are slight differences between all cases.
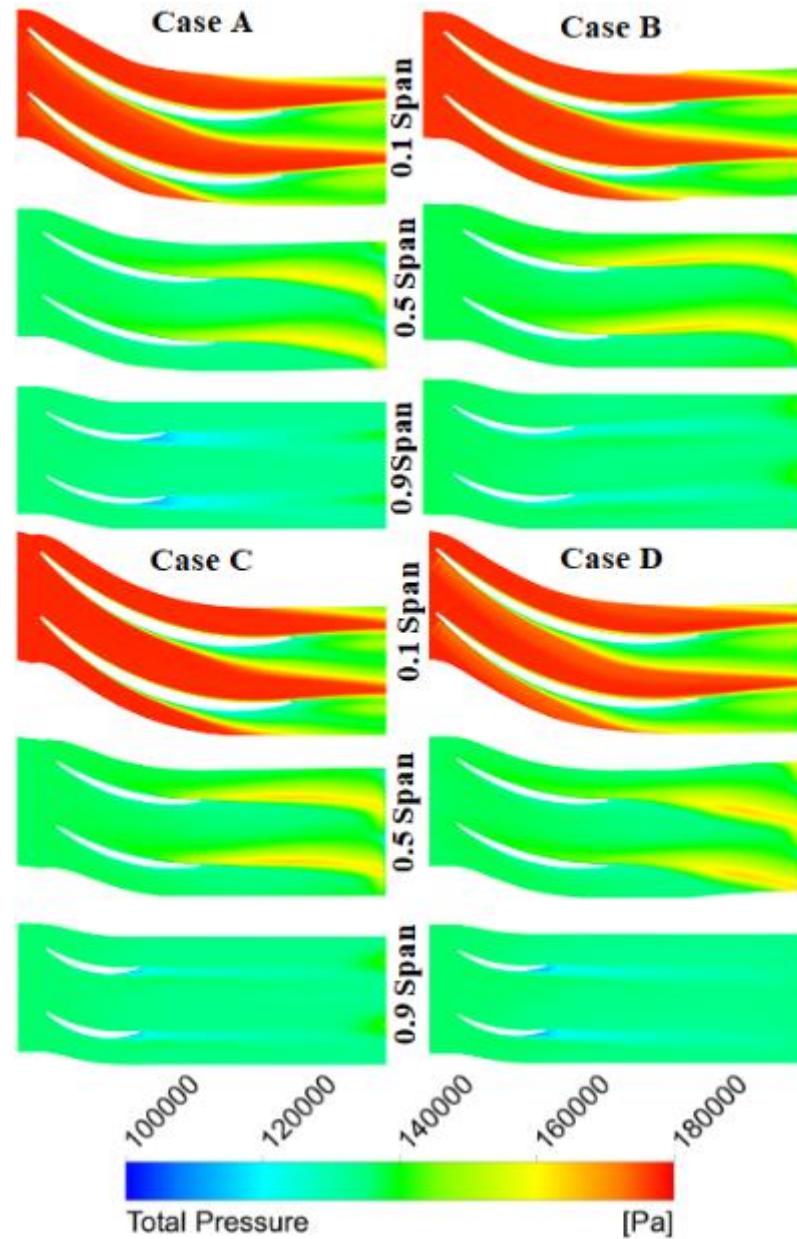


**Figure 4.15.** Total Pressure contours at 0.1, 0.5 and 0.9 spans for all cases

Entropy contours at 0.1, 0.5 and 0.9 spans for all cases are shown in Figure 4.16. Also, entropy chordwise distribution at 0.9 (top), 0.5 (mid) and 0.1 (bottom) spans were examined in order to see the difference between stator states more clearly (Figure 4.17). There are slight differences between all cases.
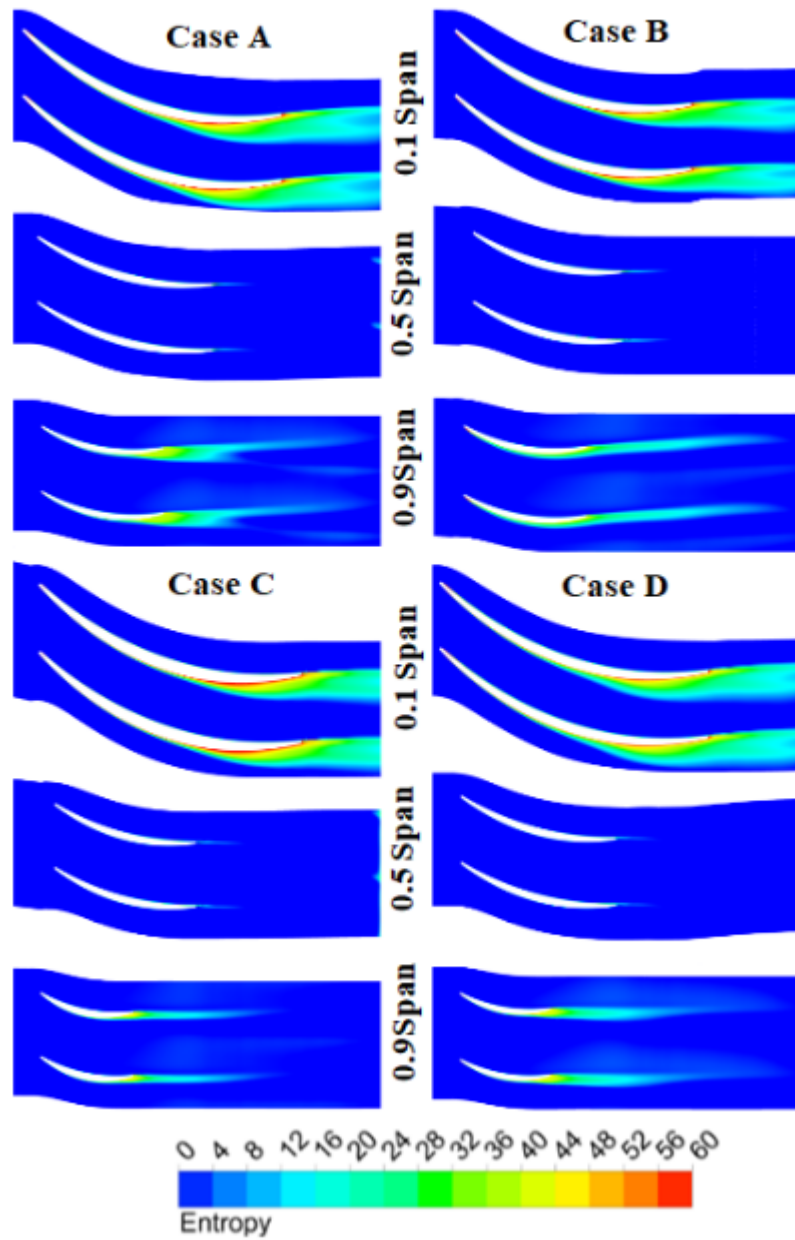
**Figure 4.16.** Entropy contours at 0.1, 0.5 and 0.9 spans for all cases
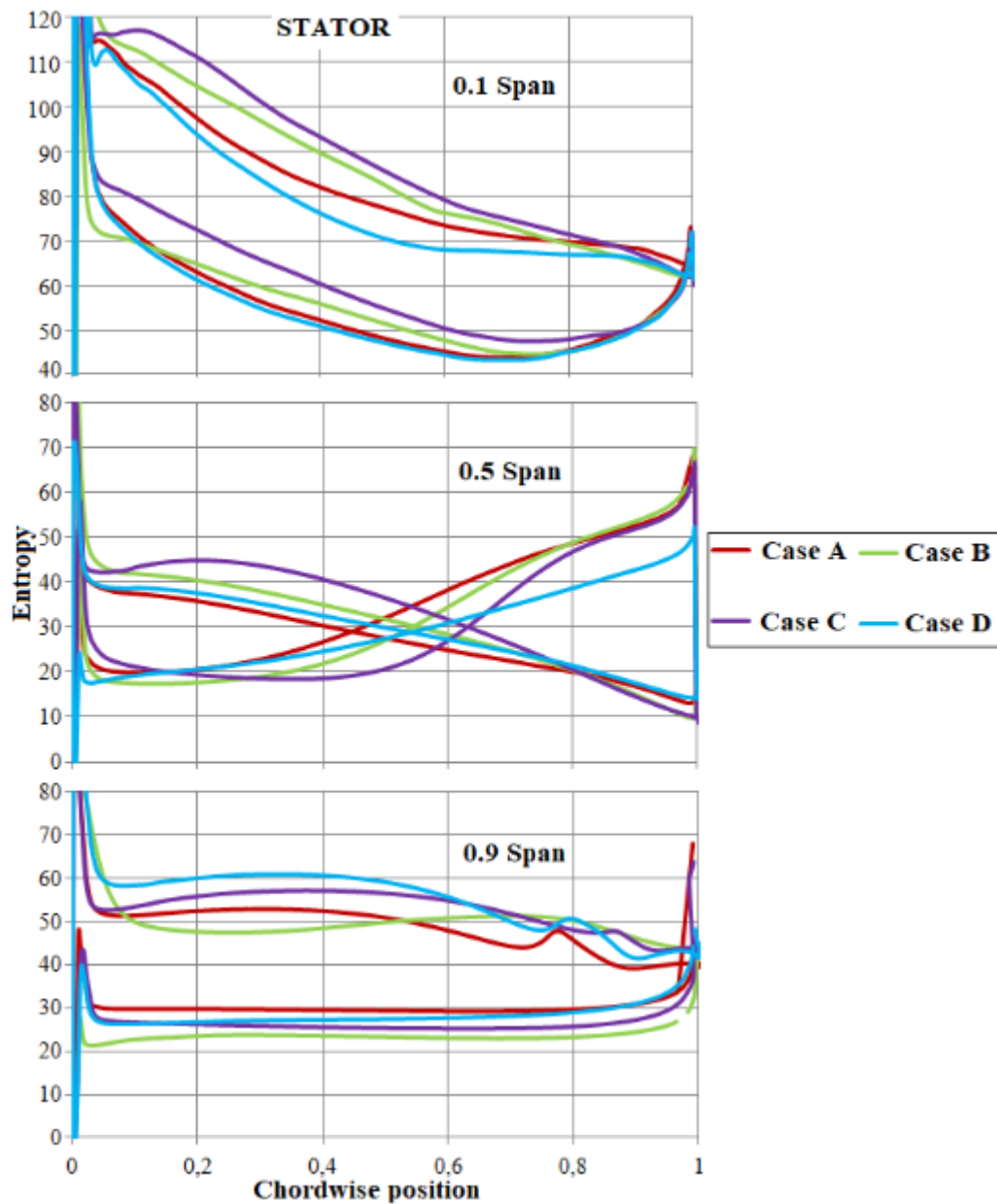
**Figure 4.17.** Entropy chordwise distribution for case A, case B, case C, and case D at the 0.9 (top), 0.5 (mid), and 0.1 (bottom) spans

Meridional view total pressure contours for Case A, Case B, Case C, and Case D are shown in Figure 4.18.
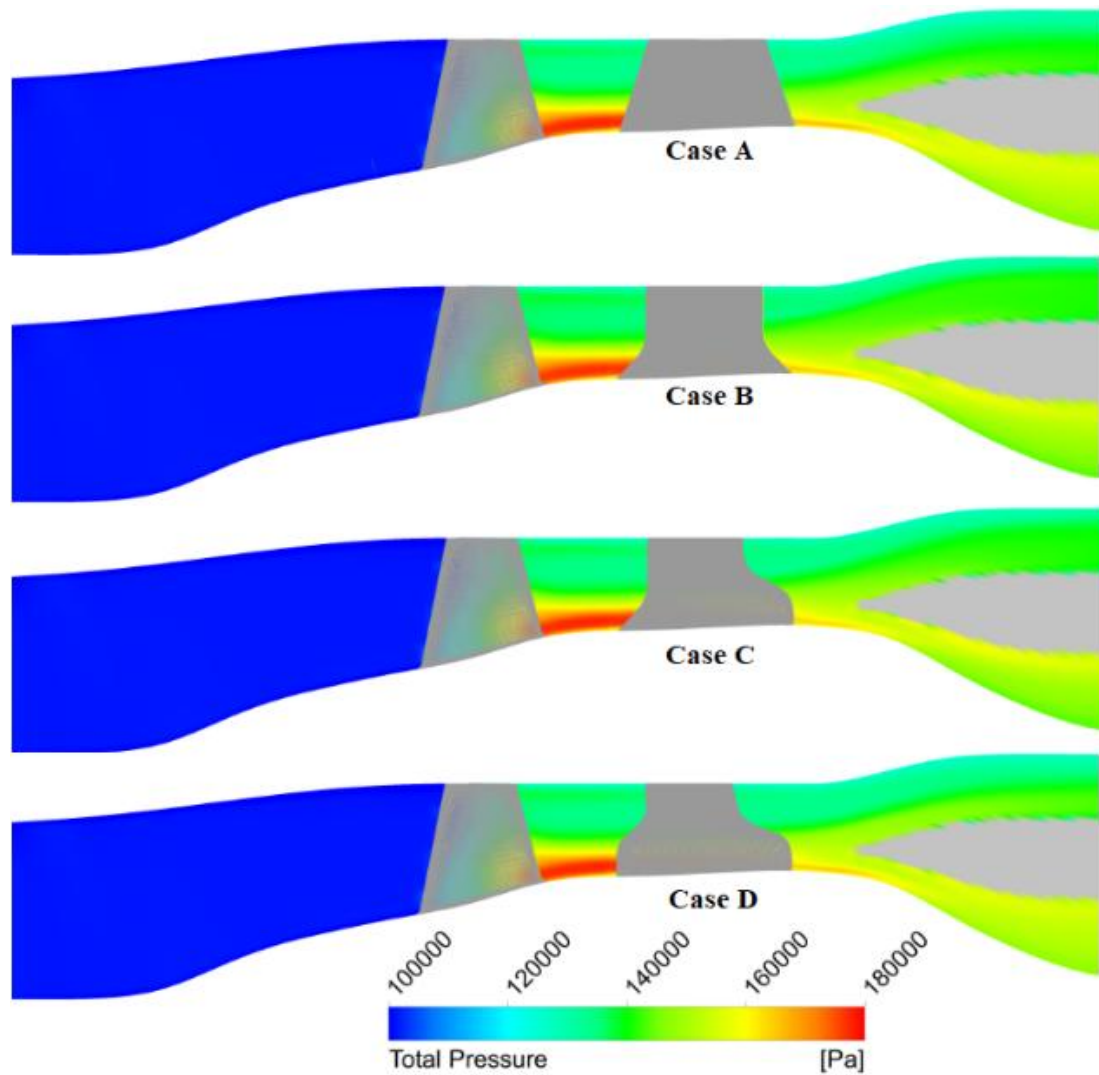
**Figure 4.18.** Meridional View Total Pressure contours for Case A, Case B, Case C, and Case D

Streamlines on stator blade SS (Suction Side) and PS (Pressure Side) for Case A, Case B, Case C, and Case D are shown in Figure 4.19. In all stator cases, the reattachment line occurs at the leading edge at the hub region. In all stator cases, radial migration occurs at the trailing edge at the hub region. In all stator cases, separation vortex occurs at the trailing edge at the tip region.

**Figure 4.19.** Streamlines on stator blade SS ( Suction Side) and PS (Pressure Side) for Case A, Case B, Case C, and Case D

# 5. CONCLUSIONS

In this study, unique unified booster and fan (LPC) concept were investigated in an ongoing research on future UAV engines by variable area micro turbofan and CVT geared architecture. To reduce costs and provide simplicity, the LPC must be a single-stage fan and must be operated by the turbine. In order to compensate for the lack of positive functionality provided by the boosterer, the inner pressure ratio of the fan must be considerably higher than the outer pressure ratio, although t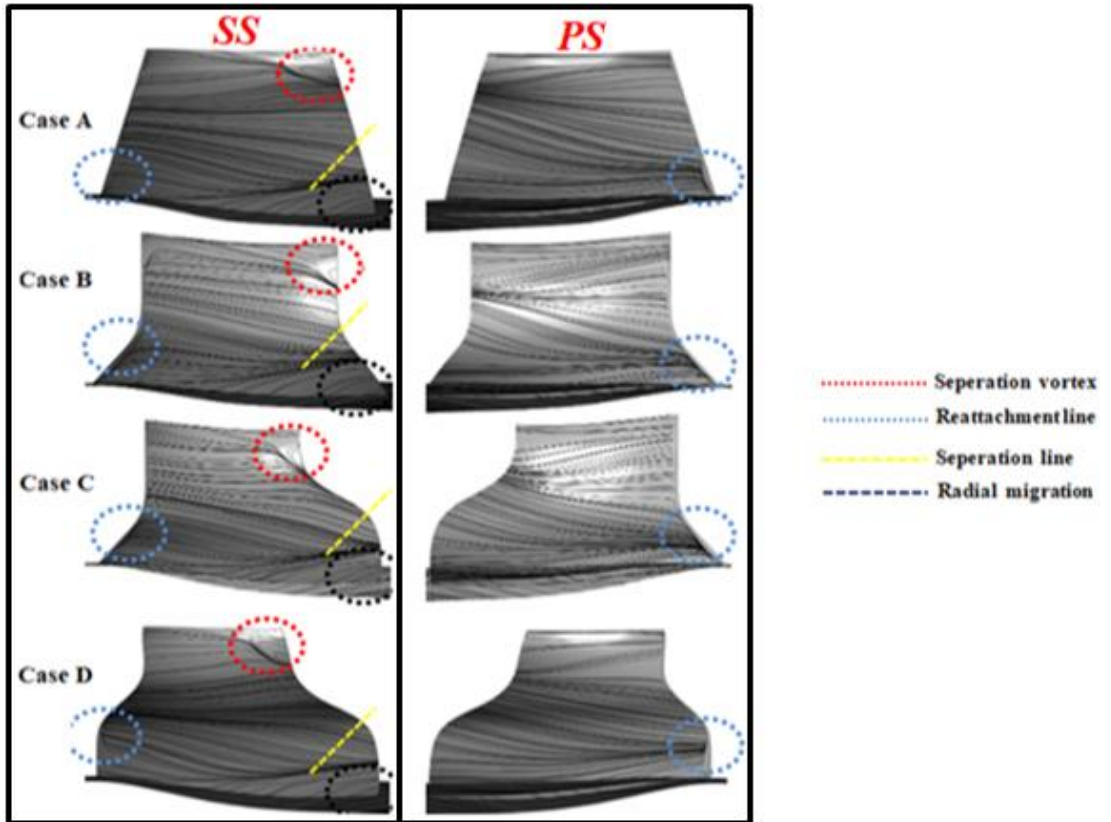he radius of the fan root is low. The summary of the accomplishments achieved in this study and the lessons learned are explained below.

Since the inner pressure ratio of the fan must be considerably higher than the bypass pressure ratio, the axial velocity at the hub increases significantly and causes to drop at the tip. The majority of the mass flux is condensed in the hub, causing shear. It also forces to reduce the channel inlet height, which task makes channel design difficult. As the rotor hub swirl increases, the flow in the stator hub becomes transonic. Furthermore, the rotor twists are significantly increased, thus adversely affecting structural integrity. Therefore, the maximum core bypass pressure ratio difference limit was initially set to 1.4 (outer stream) to 1.6 (inner stream). An alternative configuration was investigated to reduce rotor twist and stator loading. IGVs were used in front of the rotor. In the studied configuration, IGV reduced mach and stator loading, but bypass and core efficiencies decreased as much as 3%. This is due to increased shock losses and additional blading. The benefit from the alternative configuration with IGV is limited due to constraints due to radial equilibrium and choke limit. Given the interaction of undesirable shock and IGV, increased risk of choke and increased cost, the alternative configuration using this IGV was found to be less favorable. When considering the miniature dimensions, the blades are designed with a very wide chord in order to obtain reasonable thicknesses and maximum Reynolds number. Firstly, preliminary investigation has been made on meridional fluid dynamics. The concept was then designed with validated CFD

simulations and improvements were made and examined in detail. The design goals were achieved at the stator TE. However, wake mixing downstream of the high-loaded stator offers a bottleneck on performance of inner stream. For example, at the stator Te, the stage efficiency is 87%, while at three chord downstream of the stator is reduced to 79%. This means that the total pressure ratio is 1.6 at the stator TE and 1.51 at the distance of three chords downstream. In conclusion, this study focuses on stator. In addition to the stator geometry designed in the preliminary study, three stator geometries with high hub solidities were examined. Two of these stator studies have reduced tip solidities due to low tip pressure ratio, and another configuration has sweep and lean properties to reduce mixing losses and hub loading. Case D has low tip solidity and high hub solidity. Therefore, Case D was selected from the stator cases examined.

# REFERENCES

1. Cirigliano D, Frisch AM, Liu F, Sirignano WA. Diesel, Spark-Ignition, and Turboprop Engines for Long-Duration Unmanned Air Flights. Journal of Propulsion and Power. 2017;34(4):878-892. doi: https://doi.org/10.2514/1.B36547

2. Toal DJ, Keane AJ, Benito D, Dixon JA, Yang J, Kill N. Multifidelity multidisciplinary whole-engine thermomechanical design optimization. Journal of Propulsion and Power. 2014;30(6):1654-1666. doi: https://doi.org/10.2514/1.B35128

3. Goulas A, Donnerhack S, Flouros M, Misirlis D, Vlahostergios Z, Yakinthos K. Thermodynamics cycle analysis, pressure loss, and heat transfer assessment of a recuperative system for aero-engines. Journal of Engineering for Gas Turbines and Power. (2015);137(4):041205. doi: https://doi.org/10.1115/1.4028584

4. Xu L, Kyprianidis KG, Grönstedt TU. Optimization study of an intercooled recuperated aero-engine. Journal of Propulsion and Power. 2013;29(2):424-432. doi: https://doi.org/10.2514/1.B34594

5. Kyprianidis KG, Rolt AM, Grönstedt T. Multidisciplinary analysis of a geared fan intercooled core aero-engine. Journal of Engineering for Gas Turbines and Power. 2014;136(1):011203. doi: https://doi.org/10.1115/1.4025244

6. Kyprianidis KG, Rolt AM. On the optimization of a geared fan intercooled core engine design. Journal of Engineering for Gas Turbines and Power. 2015;137(4):041201. doi: https://doi.org/10.1115/1.4028544

7. Alexiou A, Roumeliotis I, Aretakis N, Tsalavoutas A, Mathioudakis K. Modeling contra-rotating turbomachinery components for engine performance simulations: the geared turbofan with contra-rotating core case. Journal of Engineering for Gas Turbines and Power. 2012;134(11):111701. doi: https://doi.org/10.1115/1.4007197

8. Speak T, Sellick R, Kloos V. Dual drive booster for a two-spool turbofan performance effects and mechanical feasibility. J Eng Gas Turbines Power. 2016;138:022603.

9. Kaiser S, Seitz A, Donnerhack S, et al. Composite cycle engine concept with hectopressure ratio. J Propul Power. 2015;32:1413–1421. doi: https://doi.org/10.2514/6.2015-4028

10. Kadosh K, Cukurel B. Micro-turbojet to turbofan conversion via continuously variable transmission: thermodynamic performance study. Journal of Engineering for Gas Turbines and Power. 2017;139(2):022603. doi: https://doi.org/10.1115/1.4034262

11. Jeschke P and Penkner A. A novel gas generator concept for jet engines using a rotating combustion chamber. J Turbomac. 2015;137:071010.

12. Palman M, Leizeronok B, Cukurel B. Mission Analysis and Operational Optimization of Adaptive Cycle Microturbofan Engine in Surveillance and Firefighting Scenarios. Journal of Engineering for Gas Turbines and Power. 2019;141(1):011010. doi: https://doi.org/10.1115/1.4040734

13. Karadimas G. Design of high-performance fans using advanced aerodynamics codes. Journal of turbomachinery. 1988;110(4):419-425. doi: https://doi.org/10.1115/1.3262214

14. Acarer S, Özkol Ü. Off-design analysis of transonic bypass fan systems using streamline curvature through-flow method. International Journal of Turbo & Jet-Engines. 2019;36(2):137-146. doi: https://doi.org/10.1515/tjj-2016-0083

15. İlhan M, Gürbüz MT, Acarer S. Unified low-pressure compressor concept for engines of future high-speed micro-unmanned aerial vehicles. *Proceedings of the Institution of Mechanical Engineers, Part G: Journal of Aerospace Engineering*, 2019:095441001984 0968. doi: https://doi.org/10.1177%2F0954410019840968

16. ANSYS, CFX. *ANSYS CFX-Solver Theory Guide*: ANSYS, Inc. Software Documentations for Release 18.2.;2017

17. Menter FR. Review of the shear-stress transport turbulence model experience from an industrial perspective. International journal of computational fluid dynamics. 2009;23(4):305-316. doi: https://doi.org/10.1080/10618560902773387

# CURRICULUM VITAE

Menal İLHAN

20-03-1995, İzmir/TURKEY

## EDUCATION

**M.Sc  (2016-2019)**    : Mechanical Engineering, İzmir Katip Çelebi University

**B.Sc  (2012-2016)**    : Mechanical Engineering, Ege University

**P.S    (2011-2012)**    : Preparation School (English), Ege University

**List of Publications:**

- İlhan M, Gürbüz MT, Acarer S. Unified low-pressure compressor concept for engines of future high-speed micro-unmanned aerial vehicles. Proceedings of the Institution of Mechanical Engineers, Part G: Journal of Aerospace Engineering. (2019); 0954410019840968. doi: https://doi.org/10.1177%2F0954410019840968

- Gürbüz MT, İlhan M, Acarer S, Karadeniz ZH. (2019). Investigation of Radial Turbines for Wind Energy Harvesting Proceedings of the Institution of Mechanical Engineers, Part A: Journal of Power and Energy. 2019;JPE-19-0027.R1, https://doi.org/10.1177/0957650919861615

- Kırmızıgöl SF, Gürbüz MT, İlhan M, Acarer S. Magnus Etkisi ile Çalışan Model Uçak Ön Tasarımı. Journal of R&D. March 2018-1;pp.48-49, Figes Engineering (non-referee publication)

**Conference Papers**

- İlhan M, Gürbüz MT, Acarer S, Karadeniz ZH. Radyal Türbin Mimarisinin Rüzgar Enerjisi Alanında Kullanımının Doğrulanmış Sayısal Akış Benzetimleri İle İncelenmesi.21st National Heating Science and Technique Congress September 13-16, 2017, Çorum/Turkey

- Kırmızıgöl SF, Gürbüz MT, İlhan M, Acarer, S. Magnus Etkisi ile Çalışan Model İHA Tasarımı, Simülasyonları ve İmalatı. VII. National Aviation and Space Conference, September 12-14 2018, Samsun/Turkey